



HAL
open science

Middle-atmosphere dynamics observed with a portable muon detector

M. Tramontini, Marina Rosas-Carbajal, C. Nussbaum, Dominique Gibert,
Jacques Marteau

► **To cite this version:**

M. Tramontini, Marina Rosas-Carbajal, C. Nussbaum, Dominique Gibert, Jacques Marteau. Middle-atmosphere dynamics observed with a portable muon detector. *Earth and Space Science*, 2019, 6 (10), pp.1865-1876. 10.1029/2019EA000655 . insu-02275907

HAL Id: insu-02275907

<https://insu.hal.science/insu-02275907>

Submitted on 19 Sep 2019

HAL is a multi-disciplinary open access archive for the deposit and dissemination of scientific research documents, whether they are published or not. The documents may come from teaching and research institutions in France or abroad, or from public or private research centers.

L'archive ouverte pluridisciplinaire **HAL**, est destinée au dépôt et à la diffusion de documents scientifiques de niveau recherche, publiés ou non, émanant des établissements d'enseignement et de recherche français ou étrangers, des laboratoires publics ou privés.



Distributed under a Creative Commons Attribution - NonCommercial - ShareAlike 4.0 International License

Middle-atmosphere dynamics observed with a portable muon detector

M. Tramontini^{1,2}, M. Rosas-Carbajal³, C. Nussbaum⁴, D. Gibert⁵, J. Marteau¹

¹Institut de Physique Nucléaire de Lyon, UMR 5822, CNRS-IN2P3, Université de Lyon, Université Claude Bernard Lyon 1, France

²CONICET - Facultad de Ciencias Astronómicas y Geofísicas, Universidad Nacional de La Plata, Argentina

³Université de Paris, Institut de Physique du Globe de Paris, CNRS, UMR 7154, F-75238 Paris, France

⁴Swiss Geological Survey at swisstopo, Seftigenstrasse 264, CH-3084 Wabern, Switzerland

⁵Univ. Rennes, CNRS, Géosciences Rennes, UMR 6118, F-35000, Rennes, France

Key Points:

- We report muon rate variations associated to temperature changes in the middle atmosphere observed with a portable muon detector
- The effect is significant both for seasonal and short-term temperature variations, even under low-opacity conditions at mid-latitudes
- We highlight potential applications on atmosphere dynamics and the need to account for these phenomena in geophysical applications

This article has been accepted for publication and undergone full peer review but has not been through the copyediting, typesetting, pagination and proofreading process which may lead to differences between this version and the Version of Record. Please cite this article as doi:

Corresponding author: Marina Rosas-Carbajal, rosas@ipgp.fr
10.1029/2019EA000655

Abstract

In the past years, large particle-physics experiments have shown that muon rate variations detected in underground laboratories are sensitive to regional, middle-atmosphere temperature variations. Potential applications include tracking short-term atmosphere dynamics, such as Sudden Stratospheric Warmings. We report here that such sensitivity is not only limited to large surface detectors under high-opacity conditions. We use a portable muon detector conceived for muon tomography for geophysical applications and we study muon rate variations observed over one year of measurements at the Mont Terri Underground Rock Laboratory, Switzerland (opacity of ~ 700 meter water equivalent). We observe a direct correlation between middle-atmosphere seasonal temperature variations and muon rate. Muon rate variations are also sensitive to the abnormal atmosphere heating in January-February 2017, associated to a Sudden Stratospheric Warming. Estimates of the effective temperature coefficient for our particular case agree with theoretical models and with those calculated from large neutrino experiments under comparable conditions. Thus, portable muon detectors may be useful to 1) study seasonal and short-term middle atmosphere dynamics, especially in locations where data is lacking such as mid-latitudes; and 2) improve the calibration of the effective temperature coefficient for different opacity conditions. Furthermore, we highlight the importance of assessing the impact of temperature on muon rate variations when considering geophysical applications. Depending on latitude and opacity conditions, this effect may be large enough to hide subsurface density variations due to changes in groundwater content, and should therefore be removed from the time-series.

1 Introduction

First observed in 1952 using radiosonde measurements (Scherhag, 1952), Sudden Stratospheric Warmings (SSWs) are extreme wintertime circulation anomalies that produce a rapid rise in temperature in the mid to upper polar stratosphere (30-50 km). SSW effects on middle-atmosphere dynamics have lifetimes of approximately 80 days (Limpasuvan, Thompson, & Hartmann, 2004). They are the clearest and strongest manifestation of dynamic coupling throughout the whole atmosphere-ocean system (Goncharenko, Chau, Liu, & Coster, 2010; Liu & Roble, 2002; O'Callaghan, Joshi, Stevens, & Mitchell, 2014). Following a major SSW, the high altitude winds reverse to flow westward instead of their usual eastward direction. This reversal often results in dramatic surface temperature reductions in mid-latitudes, particularly in Europe, which suggests the possibility of monitoring the stratosphere for predicting extreme tropospheric weather (Thompson, Baldwin, & Wallace, 2002). The frequency of SSWs may increase due to global warming (Kang & Tziperman, 2017; Schimanke, Spanghel, Huebener, & Cubasch, 2013). While many studies have focused on the characterization of SSWs through observation and modeling dynamics at high latitude regions, observation studies at mid-latitudes are rare and could be crucial to better understand the phenomena (Sox, Wickwar, Fish, & Herron, 2016; Yuan et al., 2012).

Cosmic muons represent the largest proportion of charged particles reaching the surface of the Earth, yielding a flux of $\sim 70 \text{ m}^{-2}\text{s}^{-1}\text{sr}^{-1}$ for particles above 1 GeV (Tanabashi et al., 2018). They are a product of the primary cosmic rays interaction with the atmosphere, which produces short-lived mesons, in particular, charged pions and kaons. These particles decay into muons that easily penetrate the atmosphere and may reach the surface of the Earth. The flux of muons decreases as muons travel through an increasing amount of matter. Thus, only the most energetic muons can reach underground detectors (Gaisser, Engel, & Resconi, 2016). The muon production process requires that the parent mesons did not undergo destructive interactions with the propagating medium before they decay (Grashorn et al., 2010). Thus, changes in the atmospheric properties, in particular in its density, may have large impacts on the muon flux measured at ground level, either by affecting the parent mesons survival probabilities before decay or by affecting the rate of absorption of the muons themselves along their path down from their production level.

70 An increase in the atmospheric temperature lowers the atmospheric density. Temper-
71 ature changes in the atmosphere may therefore affect the production of muons (Gaisser et
72 al., 2016). The decrease in atmospheric density increases the mean free path of the mesons
73 and therefore their decay probability, thus increasing the muon flux. The effect is more
74 important for high-energy muons, which result from high-energy mesons with larger lifetime
75 due to time dilation and therefore with longer paths in the atmosphere. This increases their
76 interaction probability before decay (Grashorn et al., 2010), thus one expects high-energy
77 muons to be more sensitive to temperature changes. The opacity is the integrated density
78 along a travel path. It is used to quantify the amount of matter encountered by the muons
79 and is generally expressed in meter water equivalent (mwe). Detectors in high-opacity con-
80 ditions are more likely to register the effects of temperature variations in the atmosphere.
81 Notice that the low-energy muons may also be affected by temperature changes because
82 their own interaction probability with the atmosphere along their path down to the Earth
83 depends on the atmospheric density. Indeed, this effect has been observed in low opacity
84 conditions (e.g. Jourde et al., 2016), but is not relevant for detectors deeper than 50 mwe
85 (Ambrosio et al., 1997). The variations in the cosmic muon flux caused by atmospheric
86 temperature changes can be treated in terms of an effective temperature (Ambrosio et al.,
87 1997; Barrett, Bollinger, Cocconi, Eisenberg, & Greisen, 1952). This effective temperature
88 is a weighted average of the atmosphere's temperature profile, with weights related to the
89 altitudes where muons are produced (Grashorn et al., 2010).

90 Modulation of the cosmic muon flux produced by seasonal variations in the atmospheric
91 temperature have been reported for large detectors (AMANDA: Bouchta (1999), Borexino:
92 Agostini et al. (2019), Daya Bay: An et al. (2018), Double Chooz: Abrahão et al. (2017),
93 GERDA: Agostini et al. (2016), IceCube: Desiati, Tilav, Rocco, Gaisser, and Kuwabara
94 (2011), LVD: Vigorito et al. (2017), MACRO: Ambrosio et al. (1997), MINOS: Adamson et
95 al. (2010, 2014), OPERA: Agafonova et al. (2018)). Osprey et al. (2009) and Agostini et
96 al. (2019) also report that measured muon rates are sensitive to short-term variations (day
97 scale) in the thermal state of the atmosphere, such as the occurrence of SSWs. Agafonova
98 et al. (2018) observed short-term, non-seasonal variations in latitudes as low as 42° N, in
99 Italy.

100 The previously mentioned studies highlight the potential of muon measurements to
101 characterize and monitor middle atmosphere dynamics. However, all these studies were
102 conducted by large-scale, general-purpose particle detectors, specifically built for neutrino
103 and high-energy particle experiments. Most of them were placed hundreds of meters under-
104 ground, which improves data sensitivity to atmospheric effects by filtering out low-energy
105 muons. The detection surface of these systems are huge compared to portable ones, which
106 are used for geoscience applications such as characterizing the density structure of volcanoes
107 (e.g. Rosas-Carbajal et al., 2017). Recently, muon rate variations following the passage of
108 a thundercloud were reported by Hariharan et al. (2019) using a relatively large detector
109 ($6 \times 6 \times 2$ m³). To the best of our knowledge, no experiment has reported the sensitivity of
110 portable muon detectors to middle atmosphere dynamics, especially under relatively low
111 opacity conditions.

112 In this paper, we study seasonal and short-term variations in the muon rate observed
113 with a portable muon detector installed at the Mont Terri Underground Rock Laboratory
114 (Switzerland, 47.4° N). We first present our detector and the general conditions under which
115 the measurements were taken. We then analyze the variations observed and compare them
116 to atmospheric temperature and middle-atmosphere dynamics data. Finally, we discuss
117 the implications of our observations both for the atmospheric science and geophysics com-
118 munities, the latter aiming to characterize density variations in the subsurface with muon
119 data.

2 The muon detector

Our portable muon detector was conceived for geoscience applications by the DI-APHANE project (e.g., Marteau et al., 2017, 2012). It is equipped with 3 plastic scintillator matrices of 80 cm width composed by $N_x = N_y = 16$ scintillators bars, in the horizontal and vertical directions, whose interceptions define 16×16 pixels of 5×5 cm². When a muon passes through the 3 matrices (i.e., an “event” is registered), 3 hits are recorded in time coincidence, with a resolution better than 1 ns (Marteau et al., 2014), enabling us to reconstruct its trajectory from the sets of pixels fired in each matrix. We apply a selection based on the goodness of the reconstructed trajectory in order to filter out random coincidences, i.e, three coincident fired pixels that do not align. If the reconstructed trajectories using two consecutive matrices differ by more than one pixel, in either the horizontal or the vertical direction, the event is discarded. More details on the hit selection and the technique applied to determine the propagation directions of muons through the detector matrices can be found in Jourde (2015) and in Marteau et al. (2014). The distance between the front and rear matrices is set to 100 cm for this study (Fig. 1a). Because of the large volume of rock studied compared to the detector size, we admit a point-like approximation of the detector (Lesparre et al., 2010). With this approximation, given that two points are sufficient to uniquely determine a direction, events whose pair of pixels in the front and the rear matrices share the same relative direction are considered to correspond to the same trajectory. This yields a total of $(2N_x - 1) \times (2N_y - 1) = 961$ axes of observation studied (represented in Fig. 1b).

The passage of muons is detected with wave-length shifting optical fibers that transport the photons generated by the scintillators to the photomultiplier, where they are detected based on a time coincidence logic. The optoelectronic chain has been developed from high-energy particle experiments on the concept of the autonomous, Ethernet-capable, low power, smart sensors (Marteau et al., 2014). In order to support strenuous field conditions, besides being sensitive the detector is also robust, modular and transportable (Lesparre et al., 2012). In this experiment, the muon detector was deployed in the Mont Terri Underground Rock Laboratory (URL) and acquired data for 382 days between October 2016 and February 2018. The minimum and the maximum amount of rock traversed by muons registered by the detector are of approximately 200 and 500 m, respectively. Prior to the underground measurements, a calibration experiment was performed by measuring the open-sky muon flux at the zenith, from which we register a total acceptance of 1385 cm² sr for our data set (Lesparre et al., 2010).

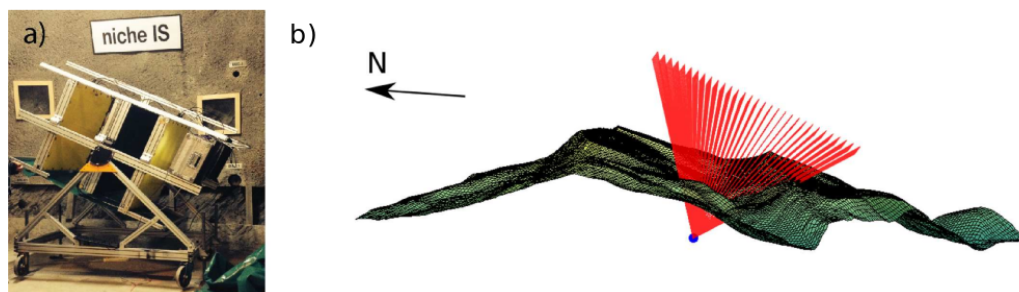


Figure 1. a) The muon telescope deployed in the Mont Terri URL. b) Telescope’s position (blue) and axes of observation (red), along with the topography.

3 Methodology

Our data set consists of a list of muon detections called “events”. Each event is characterized by the arrival time and the direction of the particle (possible directions shown in Fig. 1b). From these data, we compute the average cosmic muon rate, R , using a 30-day width Hamming moving average window (Hamming, 1998). In order to increase the signal to noise ratio and, therefore, to improve the statistics in our analysis, we merge the signals from all the directions together (e.g. Jourde et al., 2016). Such a merging is done exclusively to compute R .

Seasonal variations in R , caused by the temperature changes in the atmosphere, can be treated in terms of an effective temperature (Barrett et al., 1952), T_{eff} :

$$\frac{\Delta R}{\langle R \rangle} = \alpha_T \frac{\Delta T_{\text{eff}}}{\langle T_{\text{eff}} \rangle}, \quad (1)$$

where α_T is the effective temperature coefficient, $\langle R \rangle$ is the mean muon rate and $\langle T_{\text{eff}} \rangle$ is the mean effective temperature. T_{eff} is defined as the temperature of an isothermal atmosphere that produces the same meson intensities as the actual atmosphere. Thus, it is related to the atmosphere’s temperature profile, and it is associated to the altitudes where observed muons are produced. We use the parametrization given by Grashorn et al. (2010):

$$T_{\text{eff}} = \frac{\int_0^\infty W(X)T(X)dX}{\int_0^\infty W(X)dX}, \quad (2)$$

where the temperature, $T(X)$, is measured as a function of atmospheric depth, X . The weights, $W(X)$, contain the contribution of each atmospheric depth to the overall muon production. These weights depend on the threshold energy E_{th} , that is, the minimum energy required for a muon to survive a particular opacity in order to reach the underground detector. Since $T(X)$ is measured at discrete levels of X , we perform a numerical integration based on a quadratic interpolation between temperature measurements to obtain T_{eff} .

The effective temperature will be different for different zenith angles. To compare T_{eff} variations to our measured muon rates, we need to account for this dependence. Following Adamson et al. (2014), we bin the zenith angle distribution and calculate a weighted effective temperature, $T_{\text{eff}}^{\text{weight}}$, as:

$$T_{\text{eff}}^{\text{weight}} = \sum_{i=1}^M F_i \cdot T_{\text{eff}}(\theta_i), \quad (3)$$

where M is the number of zenith-angle bins, $T_{\text{eff}}(\theta_i)$ is the effective temperature in bin i and F_i is the fraction of muons observed in that bin. The formula for $T_{\text{eff}}(\theta_i)$ is similar to Eq. (2), but the atmospheric depth is replaced by $X/\cos\theta$ and E_{th} is calculated for each zenith angle as well. From now on, we will refer to $T_{\text{eff}}^{\text{weight}}$ as T_{eff} . These values are calculated four times a day and then day-averaged, and the resulting standard deviation is used as an uncertainty estimate of the effective temperature daily mean value. Thus, a representative value of effective temperature is calculated for each day, which fully accounts for the particular setup of our experiment.

The goodness of fit of the linear relationship in Eq. (1) can be quantified by the Pearson correlation coefficient r . This parameter is equal to ± 1 for a full positive/negative linear correlation, respectively, and 0 for no correlation. We perform a linear regression between the relative muon rate and effective temperature variations using Monte Carlo simulations. In this way, we can account for error bars in both variables and compute the uncertainty of the fitted parameters. Following Adamson et al. (2010), the intercept is fixed at zero and

193 the slope of the linear fit is the effective temperature coefficient, α_T . To evaluate the effects
 194 of systematic uncertainties we modify $\langle T_{\text{eff}} \rangle$ and the parameters involved in the computation
 195 of T_{eff} (i.e. the twelve input parameters in $W(X)$, c.f. Adamson et al., 2010) and recalculate
 196 the effective temperature coefficient, α_T . These systematic errors are added in quadrature
 197 to the statistical error obtained from the linear fit in order to obtain the experimental value
 198 of α_T .

99 We also use Monte Carlo simulations to determine the theoretical expected value of the
 200 effective temperature coefficient, α_T^{theory} , in order to compare it with the experimental one.
 201 Muon energy, E_μ , and zenithal angle, θ , are randomly sampled from the differential muon
 202 spectrum given by Gaisser et al. (2016) and corrected for altitude according to Hebbeker
 203 and Timmermans (2002). Then, the muon is randomly assigned an azimuthal angle, ϕ ,
 204 according to a uniform probability distribution. The overburden opacity in the Mont Terri
 205 URL is determined for each combination of (ϕ, θ) from our muon data set, together with the
 206 corresponding E_{th} (Tanabashi et al., 2018). We continue the Monte Carlo sampling until
 207 we obtain 10,000 successful events that satisfy $E_\mu > E_{\text{th}}$, for which we compute the α_T^{theory}
 208 distribution using the expression derived by Grashorn et al. (2010). Next, we determine the
 209 value of α_T^{theory} and its uncertainty as the mean and standard deviation of the distribution,
 210 respectively. The systematic uncertainty is the one reported by Adamson et al. (2014).

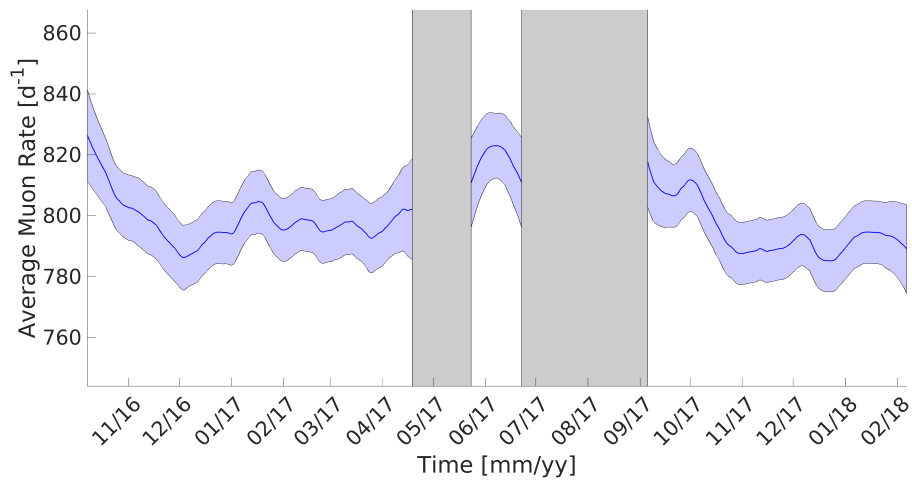
211 We look for the occurrence of SSWs during the acquisition period using the definition
 212 of a major SSW given by Charlton and Polvani (2007). A major mid-winter warming is
 213 considered to occur when the zonal mean zonal wind at 60°N and 10 hPa become easterly
 214 during winter. The first day on which this condition is met is defined as the central date of
 215 the warming. The zonal mean zonal wind is the average east-west (zonal) wind speed along
 216 a latitude circle. To ensure that only major mid-winter warmings are identified, cases where
 217 the zonal mean zonal wind does not reverse back to westerly for at least 2 weeks prior to
 218 their seasonal reversal to easterly in spring are assumed to be final warmings, and as such
 219 are discarded. SSWs typically manifest as a displacement or a splitting of the polar vortex
 220 (Charlton & Polvani, 2007), a cyclone residing on both of the Earth's poles that goes from
 221 the mid-troposphere into the stratosphere.

222 4 Results

223 Based on 382 days of data, the average daily rate of cosmic muons in the Mont Terri
 224 URL is of $(800 \pm 10) \text{ d}^{-1}$, calculated by counting all the muons detected each day no
 225 matter their direction or the altitude at which they were produced. We also compute an
 226 average muon rate for each axis of observation, which we use to estimate the corresponding
 227 opacity values. Minimum and maximum opacities are of approximately 500 and 1500 mwe,
 228 respectively, while the average opacity considering all possible directions is of (700 ± 160)
 229 mwe. The cosmic muon rate presents significant variations in time (Fig. 2). Maximum rate
 230 values occur close to the summer periods while minimum rate values occur during winter
 231 times.

32 We use the ERA5 data set offered by the European Centre for Medium-range Weather
 233 Forecast (ECMWF), which is a climate reanalysis data set produced using 4D-Var data
 234 assimilation (Copernicus Climate Change Service (C3S), 2017). Temperature data consist
 235 of interpolated (0.25° by 0.25°) globally gridded data on 37 atmospheric pressure levels from
 236 0 to 1000 hPa, listed four times a day (00:00 h, 06:00 h, 12:00 h and 18:00 h). From this
 237 data set, we interpolate the temperature profiles at Mont Terri URL location. In Fig. 3 we
 238 present the typical atmospheric temperature profiles at Mont Terri for summer, winter and
 239 a year average over the analysis period. We also display in the same plot the corresponding
 240 normalized weighting coefficients W as a function of pressure levels, used to compute T_{eff} .
 241 The largest temperature changes occur above ~ 16 km, where the weighting coefficients are
 242 more significant. The effective temperatures corresponding to the average curves and $\theta = 0^\circ$

243 are given by $T_{\text{eff}}^{\text{year}} = (217 \pm 1)$ K, $T_{\text{eff}}^{\text{summer}} = (225 \pm 1)$ K and $T_{\text{eff}}^{\text{winter}} = (214 \pm 1)$ K. There
 244 is thus a difference of ~ 10 K between typical summer and winter conditions.



245 **Figure 2.** Average cosmic muon rate as a function of time, computed using a 30-day width
 246 Hamming moving average window. The colored surface delimits the 95% confidence interval. Gray
 47 bars indicate periods where the acquisition was interrupted for work in the Mont Terri URL.

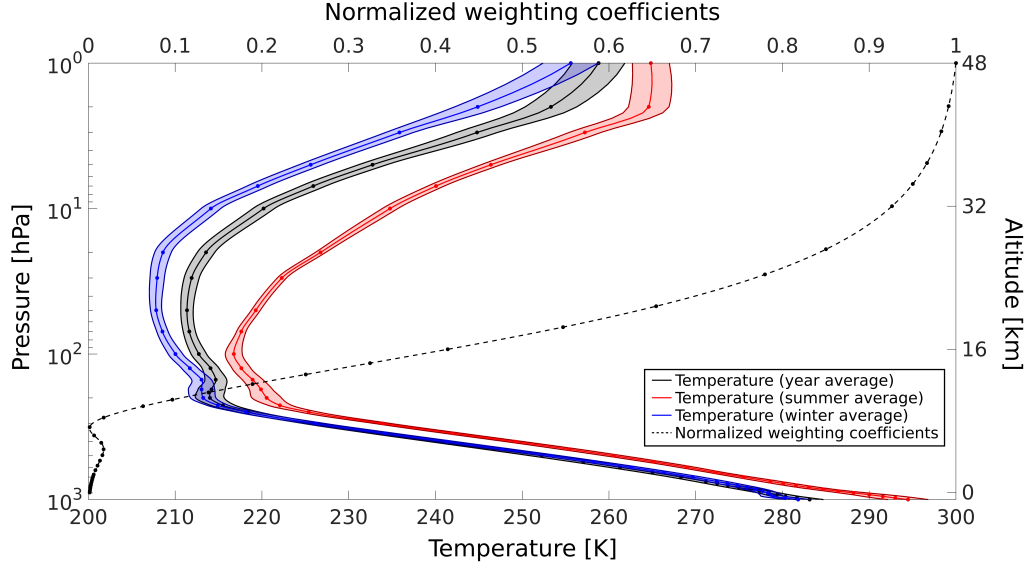
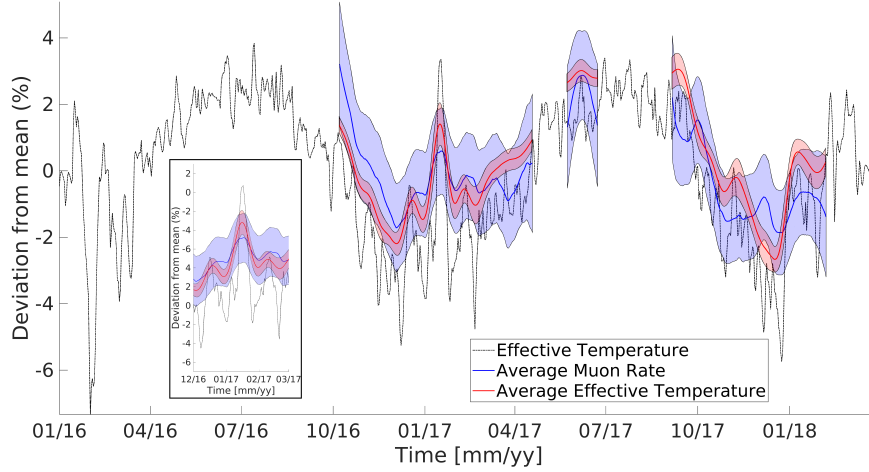
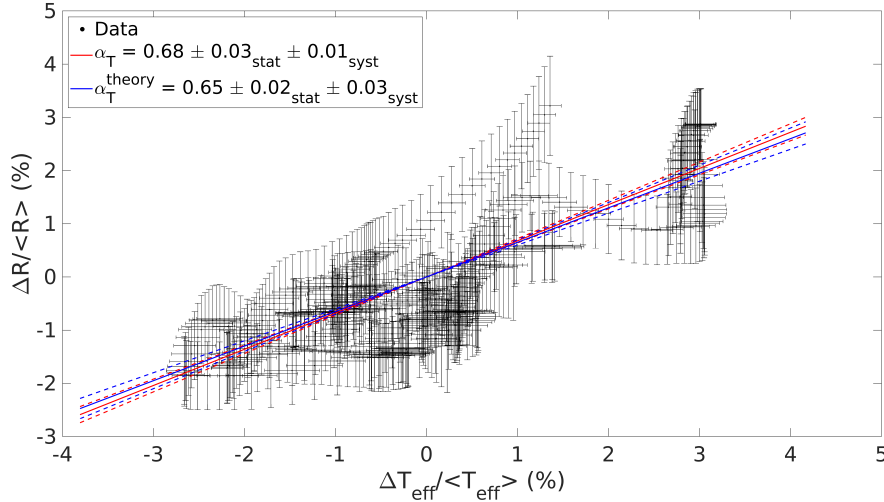


Figure 3. Atmospheric temperature profiles (solid lines) above the Mont Terri site, and weighting coefficients (dashed line) used to calculate T_{eff} , as a function of pressure level and altitude. The dots represent the 37 pressure levels for which the temperature data sets are provided by the ECMWF. The right vertical axis represents approximate altitudes corresponding to the pressure levels on the left vertical axis. The summer average temperature (solid red line) and the winter average temperature (solid blue line) are computed considering a period of 1.5 months in each season during 2017. The colored surfaces represent the ± 1 standard deviation in each curve. The effective temperatures of each profile are: $T_{\text{eff}}^{\text{year}} = (217 \pm 1)$ K, $T_{\text{eff}}^{\text{summer}} = (225 \pm 1)$ K and $T_{\text{eff}}^{\text{winter}} = (214 \pm 1)$ K.

We compare the variations in the muon rate to the variations in the effective temperature in Fig. 4 in terms of relative variations (see Eq. 1). For consistency, we also apply a Hamming moving average window of 30 days to the T_{eff} time series. The two average curves evolve similarly in time. Indeed, the Pearson correlation coefficient between the deviation from mean of the average muon rate and that of average effective temperature yield a value of 0.81. We compute a linear fit between the two data sets (see Methodology), which yields an effective temperature coefficient of $\alpha_T = 0.68 \pm 0.03_{\text{stat}} \pm 0.01_{\text{syst}}$, with $\chi^2/\text{NDF} = 414/381$ being the reduced χ^2 of the fit (Fig. 5). The largest contribution to the systematic error in α_T comes from the ± 0.06 uncertainty in the meson production ratio (Barr, Robbins, Gaisser, & Stanev, 2006), the ± 0.31 K uncertainty in the mean effective temperature (Adamson et al., 2010) and the ± 0.026 TeV uncertainty in E_{th} , which results from the distribution of opacities along the axes of observation. To discard possible systematic biases, we also performed a linear fit allowing for a non-zero y intercept. The fit resulted in an estimated value of zero within one standard deviation uncertainty for this intercept, and a slightly lower value of $\alpha_T = 0.67 \pm 0.03_{\text{stat}} \pm 0.01_{\text{syst}}$ for the effective temperature coefficient.



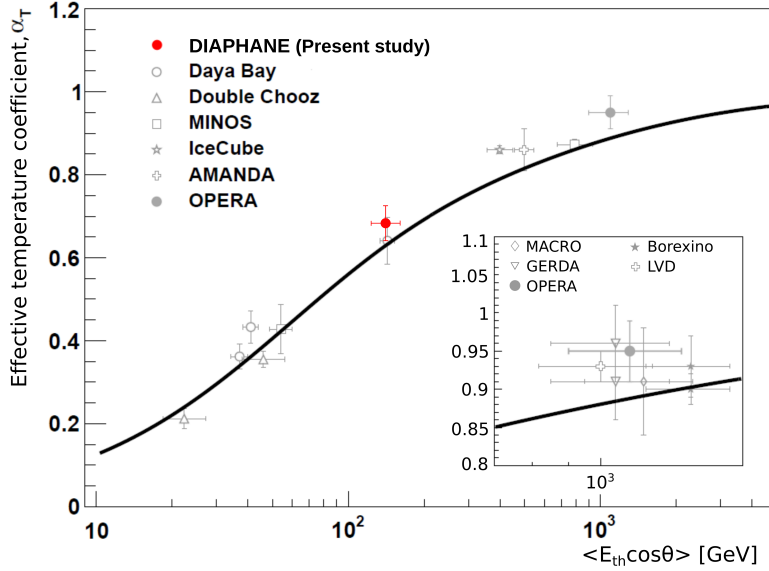
273 **Figure 4.** Daily percent deviations from the mean of the average cosmic muon rate, the daily
 274 effective temperature, and the average effective temperature computed using a 30 days width Ham-
 275 ming moving average window. The colored surfaces delimit the 95% confidence interval associated
 276 to each curve. The inset displays a zoom around the period of time in which a major SSW is
 277 detected.



278 **Figure 5.** Average cosmic muon rate relative variation versus average effective temperature
 279 relative variation, fitted with a line with the y -intercept fixed at 0. The resulting slope is $\alpha_T =$
 280 $0.68 \pm 0.03_{stat} \pm 0.01_{syst}$ and is represented with a red line. The blue line represents the theoretical
 281 expected value of $\alpha_T^{theory} = 0.65 \pm 0.02_{stat} \pm 0.03_{syst}$. The dotted lines represent the uncertainty
 282 of each one of the values.

283 The theoretical expected value was found to be $\alpha_T^{theory} = 0.65 \pm 0.02_{stat} \pm 0.03_{syst}$.
 284 Thus, the experimentally estimated value is consistent with the theoretical one within one
 285 standard deviation. In Fig. 6 we present our estimated value of α_T along with a theoretical

286 model accounting for pions and kaons (Agafonova et al., 2018), and estimates from other
 287 experiments. Our estimate is consistent with the one obtained by An et al. (2018) in similar
 288 opacity conditions, and with the theoretical model.

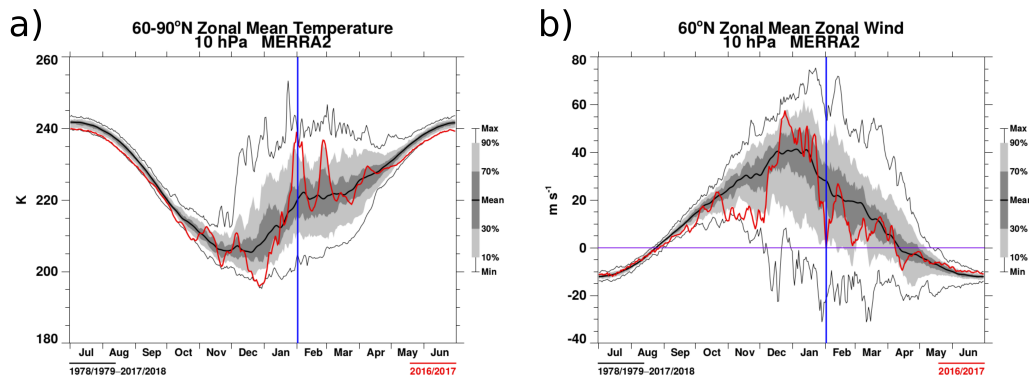


289 **Figure 6.** Experimental values of the effective temperature coefficient as a function of $\langle E_{th} \cos \theta \rangle$.
 290 The red dot represents the present study. The continuous black line represents a theoretical model.
 291 The insert plot show the experiments performed at the underground Gran Sasso Laboratory. Figure
 292 adapted from Agafonova et al. (2018)

293 Taking a closer look at Fig. 4, we can see that an anomalous increase in the effective
 294 temperature occurs between January and February 2017. The same anomalous behavior
 295 can be observed in the muon rate (see inset in Fig. 4). We used the Charlton and Polvani
 296 (2007) definition and the Modern-Era Retrospective analysis for Research and Applications,
 297 Version 2 (MERRA-2), produced by the Goddard Earth Observing System Data Assimilation
 298 System (GEOS DAS) (Gelaro et al., 2017) to determine if a major SSW occurred
 300 during this time period. We found that a major SSW took place during winter 2016-2017,
 301 with February 1 as the central date of the warming. In a few days, it increased the zonal
 mean temperature in the polar region by more than 20 K (Fig. 7 a).

302 Finally, we analyzed changes produced by the SSW using Ertel’s potential vorticity
 303 (Matthewman, Esler, Charlton-Perez, & Polvani, 2009). This parameter quantifies the
 304 location, size, and shape of the winter polar vortex. Figure 8 shows the spatial distribution
 305 of Ertel’s potential vorticity at the 850 K potential temperature surface (~ 10 hPa, ~ 32
 306 km) for 3 different days, which are representative of the changes provoked. The figure also
 307 shows the effective temperature spatial distribution during these 3 days. On January 1 (Fig.
 308 a) the vorticity and temperature exhibit “typical” winter conditions: the polar vortex is
 309 centered on the Pole, together with the minimum effective temperature. On January 17,
 310 a reshaping on the polar vortex can be already observed. It is at this moment also that
 311 the largest effective temperature anomaly occurs in the Mont Terri region (Fig. 8 b). On
 312 February 2, that is, one day after the event can be properly classified as a major SSW
 313 due to the reversal of the zonal mean zonal wind (see Fig. 7 b), the polar vortex shape is
 314 still anomalous with the “comma” shaped maximum of potential vorticity now closer to the

315 Mont Terri URL (Fig. 8 c). At the same time, the effective temperature in the Mont Terri
 316 region has decreased to values similar to those in January 1.



17 **Figure 7.** GEOS DAS MERRA-2 data used to define SSW events. a) zonal mean temperatures
 318 averaged over 60°N-90°N. b) zonal mean zonal wind at 60°N. The red curve denotes values for the
 19 2016-2017 period and the thick black curve corresponds to climatological values averaged from 1978
 320 to 2018. The vertical blue lines reference a major SSW for that winter.

326 5 Discussion

327 After a year of continuous muon measurements with a portable muon detector under
 28 relatively low-opacity conditions, we found that changes in the thermal state of the atmo-
 329 sphere represent the largest cause of muon rate variations. The correlation between these
 330 variables was first suggested by a simple comparison of the relative variation time-series.
 31 Then, it was confirmed by the large correlation coefficient (0.81), and by the fitted effec-
 332 tive temperature coefficient, which is in agreement with the theoretical value predicted for
 333 our particular opacity and zenith angle conditions. Furthermore, our experiment was by
 34 chance performed under similar opacity conditions to the Daya Bay detector, an established
 335 underground muon detector especially built for neutrino experiments (An et al., 2018). Its
 336 corresponding estimate of the effective temperature coefficient is also in agreement with ours
 37 (Fig. 6).

339 Our muon detector is sensitive to both seasonal and short-term temperature variations.
 40 The regional thermal anomaly reaching its maximum around January 17, 2017 (Fig. 4),
 41 is coincident with the polar vortex changing its shape from a normal pole-centered circle
 342 to a displaced “comma shaped” one (Fig. 8). This is a typical feature of a SSW (O’Neill,
 343 2003). Furthermore, the criteria by Charlton and Polvani (2007) for declaring a major SSW
 44 is accomplished 15 days later. The time difference can be potentially explained by the
 345 zonally-averaged wind criteria used to define major SSWs, against the local character of the
 temperature variations affecting the production of high-energy muons.

46 Under much higher opacity conditions (3,800 in mwe, i.e., more than 5 times the Mont
 47 Terri URL opacity), the large muon detector of the Borexino experiment, Gran Sasso, Italy,
 348 also reported muon rate variations related to this SSW in 2017 (Agostini et al., 2019).
 49 Given the large opacity, most of the muons completely lose their energy before reaching
 50 the detector. Thus, only high-energy muons resulting from the decay of high-energy parent
 351 mesons are detected. As explained by Grashorn et al. (2010), high-energy mesons are
 352 most sensitive to middle-atmosphere temperature variations due to their relatively longer
 53 lifetime, and thus a higher probability of interacting with the atmosphere before decaying.

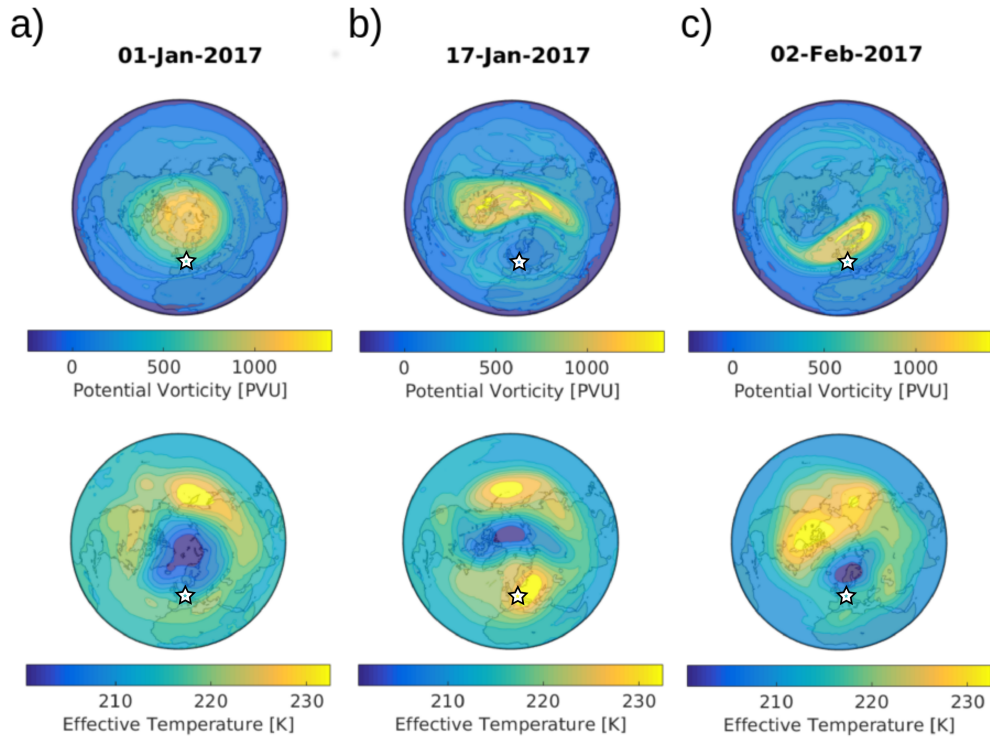


Figure 8. Potential vorticity at the 850 K potential temperature surface (top) and effective temperature (bottom) for January 1, January 17 and February 2, 2017, derived from the ECMWF data set. The maps are centered on the North Pole and the location of the Mont Terri Underground Laboratory (47.38°N, 7.17°E), close to the town of Saint-Ursanne, Switzerland, is represented with a star. $1 \text{ PVU} = 10^{-6} \text{ K m}^2 \text{ Kg}^{-1} \text{ s}^{-1}$.

This results in a higher sensitivity to temperature variations, which translates into a larger effective temperature coefficient (see Fig. 6). Despite being in less advantageous conditions in terms of detector acceptance and tunnel depth, our portable muon detector was also able to detect these short-term effect (15-days) directly linked to middle-atmosphere dynamics (Fig. 4).

Compared to lidar measurements, which can obtain temperature profiles over tens of kilometers in altitude but have very narrow global coverage (only as wide as the laser beam), muon detectors naturally provide integrated measurements in altitude, and a larger horizontal coverage. Our results therefore imply that small and affordable muon detectors could be used to study middle-atmosphere temperature variations without resorting to, for example, expensive lidar systems. Besides being transportable, the advantage is that no high-opacity conditions are needed. A minimum opacity of 50 mwe would be required to filter out the temperature-dependent lowest-energy muons (Grashorn et al., 2010). Besides being temperature dependent, low-energy muons can also be influenced by other phenomena such as atmospheric pressure variations (Jourde et al., 2016), which is why we consider optimal to remove them. However, open-sky conditions may also reveal new insights into atmospheric phenomena (e.g., Hariharan et al. (2019)) and more experimental studies are needed to better understand the limits of the methodology. Thus, detectors could be installed in any buried facility with access to electrical power and real-time data transmission, for example

with a wi-fi network., such as road tunnels. In Europe, many underground research facilities exist in this condition (e.g. Mont Terri UL in Switzerland, 47.4°N; the LSBB UL in France, 43.9°N; Canfranc UL in Spain, 42.7°N). These experiments could be crucial to fill the current data gap related to middle-atmospheric dynamics, in particular the study of temperature anomalies associated to SSW in mid-latitudes (Sox et al., 2016). Furthermore, the technique may be used to study similar phenomena in the Southern Hemisphere.

The effective atmospheric temperature to which the muon rate is sensitive is a weighted average of a temperature profile from 0 to 50 km, with increasingly significant weights at higher altitudes (Grashorn et al., 2010). Indeed, 70 % of the total weights are given between 50 and 26 km, 90 % between 50 and 18 km and 95 % between 50 and 15 km (see Fig. 3). Thus, muon rate variations are mostly sensitive to temperature variations in the high stratosphere. Muon measurements can therefore complement lidar mesospheric studies (e.g., Sox et al. (2016); Yuan et al. (2012)). In terms of the spatial support, in the configuration used for this experiment (see Section 2), the total angular aperture of the detector is of approximately $\pm 40^\circ$, but more than 95% of the muons are registered within an aperture of $\pm 30^\circ$. At 50 km, this represents a surface of $50 \times 50 \text{ km}^2$. Therefore, muon measurements may be used to sample more regional atmospheric behavior.

Besides the potential applications to atmospheric studies, portable muon detectors may be used to precisely calibrate the effective temperature curve (Fig. 6). The experimental setups used to estimate these values, so far, are concentrated in either high or low-opacity conditions, whereas with our approach we could sample the curve rather uniformly, even in the same tunnel by varying the orientation of our detector and thus the opacity and zenith angle conditions.

Our findings have direct implications for applications aiming to characterize density variations in the subsurface (e.g. Jourde et al. (2016)). Indeed, synchronous tracking of the open-sky muon rate while performing a continuous imaging of a geological body (e.g. density monitoring) may not be sufficient to characterize the influence of high-atmosphere temperature variations since the relative effect on the total amount of muons registered increases with opacity. In turn, the mentioned possibility to improve the calibration of the muon-rate dependence with middle-atmosphere dynamics will be crucial to safely remove this effect. The effect will be increasingly important at higher latitudes due to the increase of seasonal temperature variations, and for increasing rock opacities. At Mont Terri (47.38°N), relative effective temperature variations can be as high as 4%, which given the effective temperature coefficient estimated, imply changes in muon rate as high as 3% (c.f. Fig. 4). However, muon rate changes would be at maximum 1% if the opacity would be reduced by one order of magnitude to 70 mwe, or equivalently 26 m of standard rock, and for vertical observations.

Finally, relative temperature and muon rate variations are not always coincident in Fig. 4, despite using the same time-averaging window. Equivalently, deviations from the linear relationship up to 2% and mostly around 1% can be observed in Fig. 5. The deviations from a perfect correspondence are presumably due to physical phenomena influencing the muon rate other than the effective atmospheric temperature. Variations arising from changes in the primary cosmic rays, or changes in the geomagnetic field induced by solar wind typically have temporal scales that are much smaller (e.g. seconds to hours) or much larger (e.g. a solar cycle of ~ 11 years). Changes reported recently as induced by lower altitude atmospheric phenomena such as thunderclouds only lasted 10 minutes (Hariharan et al., 2019), and the low-energy muons affected by atmospheric pressure variations (Jourde et al., 2016) get filtered in the first meters of rock in our experiment. A much more likely explanation may be given by changes in the groundwater content of the rock overlying the Mont Terri URL and will be the subject of forthcoming publications.

6 Conclusion

We report for the first time sensitivity to middle-atmosphere temperature variations using a portable muon detector. Changes detected are associated not only to seasonal variations but also short-term (15-days) variations caused by a Sudden Stratospheric Warming. The occurrence of this event was verified by applying a standard definition of SSWs, and also observed by regional temperature and polar vortex variations obtained from ECMWF and MERRA-2 reanalysis data. Previous reports on the sensitivity of muon rate to these phenomena exist only for large, expensive and immobile muon detectors often times associated to neutrino experiments and high-opacity conditions. Our findings imply that portable muon detectors may be used to further study short-term temperature variations, and to improve the calibration curve of muon rate dependence with an effective temperature value. This, in turn, is crucial for geoscience applications aiming at studying subsurface processes by characterizing density changes with muons.

Acknowledgments

This study is part of the DIAPHANE project and was financially supported by the ANR-14-CE 04-0001 and the MD experiment of the Mont Terri project (www.mont-terri.ch) funded by Swisstopo. MRC thanks the AXA Research Fund for their financial support. We are grateful to Thierry Theurillat and Senecio Schefer for their technical and logistical assistance at Mont Terri URL. The MERRA data are available from https://acd-ext.gsfc.nasa.gov/Data_services/met/ann_data.html, and the ECMWF data from <https://www.ecmwf.int/>. Muon data used for all calculations are displayed in figures and are available in the Supplementary Table S1. This is IPGP contribution number 4049. We thank the editor and two anonymous reviewers for their constructive comments and suggestions, which helped to improve our work.

References

- Abrahão, T., Almazan, H., Dos Anjos, J., Appel, S., Baussan, E., Bekman, I., ... others (2017). Cosmic-muon characterization and annual modulation measurement with Double Chooz detectors. *Journal of Cosmology and Astroparticle Physics*, 2017(02), 017.
- Adamson, P., Andreopoulos, C., Arms, K., Armstrong, R., Auty, D., Ayres, D., ... others (2010). Observation of muon intensity variations by season with the MINOS far detector. *Physical Review D*, 81(1), 012001.
- Adamson, P., Anghel, I., Aurisano, A., Barr, G., Bishai, M., Blake, A., ... others (2014). Observation of muon intensity variations by season with the MINOS near detector. *Physical Review D*, 90(1), 012010.
- Agafonova, N., Alexandrov, A., Anokhina, A., Aoki, S., Ariga, A., Ariga, T., ... others (2018). Measurement of the cosmic ray muon flux seasonal variation with the OPERA detector. *arXiv preprint arXiv:1810.10783*.
- Agostini, M., Allardt, M., Bakalyarov, A., Balata, M., Barabanov, I., Barros, N., ... others (2016). Flux modulations seen by the muon veto of the GERDA experiment. *Astroparticle Physics*, 84, 29–35.
- Agostini, M., Altenmüller, K., Appel, S., Atroshchenko, V., Bagdasarian, Z., Basilico, D., ... others (2019). Modulations of the Cosmic Muon Signal in Ten Years of Borexino data. *Journal of Cosmology and Astroparticle Physics*, 2019(02), 046.
- Ambrosio, M., Antolini, R., Auriemma, G., Baker, R., Baldini, A., Barbarino, G., ... others (1997). Seasonal variations in the underground muon intensity as seen by MACRO. *Astroparticle Physics*, 7(1-2), 109–124.
- An, F., Balantekin, A., Band, H., Bishai, M., Blyth, S., Cao, D., ... others (2018). Seasonal variation of the underground cosmic muon flux observed at Daya Bay. *Journal of Cosmology and Astroparticle Physics*, 2018(01), 001.
- Barr, G., Robbins, S., Gaisser, T., & Stanev, T. (2006). Uncertainties in atmospheric

- 474 neutrino fluxes. *Physical Review D*, 74(9), 094009.
- 475 Barrett, P. H., Bollinger, L. M., Cocconi, G., Eisenberg, Y., & Greisen, K. (1952). Inter-
476 pretation of cosmic-ray measurements far underground. *Reviews of Modern Physics*,
477 24(3), 133.
- 478 Bouchta, A. (1999). Seasonal variation of the muon flux seen by AMANDA. In *the proceed-*
479 *ings of the International Cosmic Ray Conference* (Vol. 2, p. 108).
- 480 Charlton, A. J., & Polvani, L. M. (2007). A new look at stratospheric sudden warmings.
481 Part I: Climatology and modeling benchmarks. *Journal of Climate*, 20(3), 449–469.
- 482 Copernicus Climate Change Service (C3S). (2017). *ERA5: Fifth generation of ECMWF*
483 *atmospheric reanalyses of the global climate*.
- 484 Desiati, P., Tilav, S., Rocco, D., Gaisser, T., & Kuwabara, T. (2011). Seasonal variations
485 of high energy cosmic ray muons observed by the Icecube observatory as a probe of
486 kaon/pion ratio. In *the proceedings of the 32nd International Cosmic Ray Conference*,
487 *August 11–18, Beijing, China*.
- 488 Gaisser, T. K., Engel, R., & Resconi, E. (2016). *Cosmic rays and particle physics*. Cambridge
489 University Press.
- 490 Gelaro, R., McCarty, W., Suárez, M. J., Todling, R., Molod, A., Takacs, L., ... others
491 (2017). The modern-era retrospective analysis for research and applications, version
492 2 (MERRA-2). *Journal of Climate*, 30(14), 5419–5454.
- 493 Goncharenko, L., Chau, J., Liu, H.-L., & Coster, A. (2010). Unexpected connections
494 between the stratosphere and ionosphere. *Geophysical Research Letters*, 37(10).
- 495 Grashorn, E., De Jong, J., Goodman, M., Habig, A., Marshak, M., Mufson, S., ... Schreiner,
496 P. (2010). The atmospheric charged kaon/pion ratio using seasonal variation methods.
497 *Astroparticle Physics*, 33(3), 140–145.
- 498 Hamming, R. W. (1998). *Digital filters*. Courier Corporation.
- 499 Hariharan, B., Chandra, A., Dugad, S., Gupta, S., Jagadeesan, P., Jain, A., ... others
500 (2019). Measurement of the electrical properties of a thundercloud through muon
501 imaging by the GRAPES-3 experiment. *Physical Review Letters*, 122(10), 105101.
- 502 Hebbeker, T., & Timmermans, C. (2002). A compilation of high energy atmospheric muon
503 data at sea level. *Astroparticle Physics*, 18(1), 107–127.
- 504 Jourde, K. (2015). *Un nouvel outil pour mieux comprendre les systèmes volcaniques: la to-*
505 *mographie par muons, application à la Soufrière de Guadeloupe* (PhD Thesis). Institut
506 de Physique du Globe de Paris (IPGP).
- 507 Jourde, K., Gibert, D., Marteau, J., de Bremond d’Ars, J., Gardien, S., Girerd, C., &
508 Ianigro, J.-C. (2016). Monitoring temporal opacity fluctuations of large structures
509 with muon radiography: a calibration experiment using a water tower. *Scientific*
510 *Reports*, 6, 23054.
- 511 Jourde, K., et al. (2016). Muon dynamic radiography of density changes induced by hy-
512 drothermal activity at the La Soufrière of Guadeloupe volcano. *Scientific Reports*, 6,
33406.
- 514 Kang, W., & Tziperman, E. (2017). More frequent sudden stratospheric warming events due
515 to enhanced MJO forcing expected in a warmer climate. *Journal of Climate*, 30(21),
516 8727–8743.
- 517 Lesparre, N., Gibert, D., Marteau, J., Déclais, Y., Carbone, D., & Galichet, E. (2010).
518 Geophysical muon imaging: feasibility and limits. *Geophysical Journal International*,
519 183(3), 1348–1361.
- 520 Lesparre, N., Marteau, J., Déclais, Y., Gibert, D., Carlus, B., Nicollin, F., & Kergosien, B.
521 (2012). Design and operation of a field telescope for cosmic ray geophysical tomogra-
522 phy. *Geoscientific Instrumentation, Methods and Data Systems*, 1, 33–42.
- 523 Limpasuvan, V., Thompson, D. W., & Hartmann, D. L. (2004). The life cycle of the
524 Northern Hemisphere sudden stratospheric warmings. *Journal of Climate*, 17(13),
525 2584–2596.
- 526 Liu, H.-L., & Roble, R. (2002). A study of a self-generated stratospheric sudden warming
527 and its mesospheric–lower thermospheric impacts using the coupled time-gcm/ccm3.
528 *Journal of Geophysical Research: Atmospheres*, 107(D23), ACL–15.

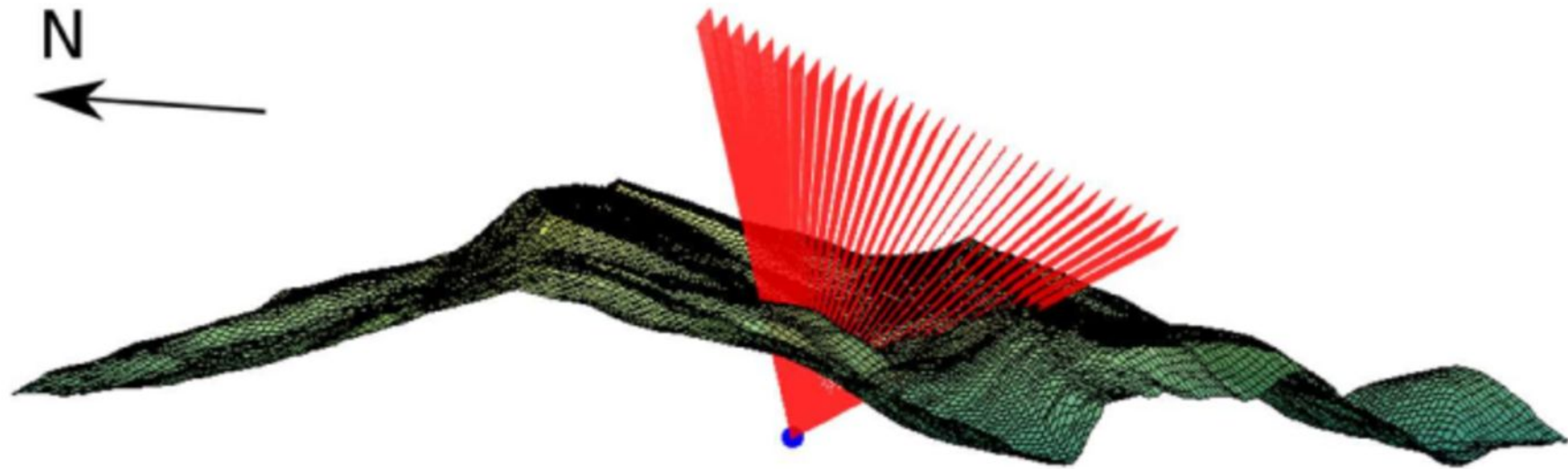
- 529 Marteau, J., de Bremond d'Ars, J., Gibert, D., Jourde, K., Gardien, S., Girerd, C., &
530 Ianigro, J.-C. (2014). Implementation of sub-nanosecond time-to-digital convertor in
531 field-programmable gate array: applications to time-of-flight analysis in muon radio-
532 graphy. *Measurement Science and Technology*, *25*(3), 035101.
- 533 Marteau, J., de Bremond d'Ars, J., Gibert, D., Jourde, K., Ianigro, J.-C., & Carlus, B.
534 (2017). DIAPHANE: Muon tomography applied to volcanoes, civil engineering, ar-
535 chaeology. *Journal of Instrumentation*, *12*(02), C02008.
- 536 Marteau, J., Gibert, D., Lesparre, N., Nicollin, F., Noli, P., & Giacoppo, F. (2012). Muons
537 tomography applied to geosciences and volcanology. *Nuclear Instruments and Methods
538 in Physics Research Section A: Accelerators, Spectrometers, Detectors and Associated
539 Equipment*, *695*, 23–28.
- 540 Matthewman, N. J., Esler, J. G., Charlton-Perez, A. J., & Polvani, L. M. (2009). A new
541 look at stratospheric sudden warmings. Part III: Polar vortex evolution and vertical
542 structure. *Journal of Climate*, *22*(6), 1566–1585.
- 543 O'Callaghan, A., Joshi, M., Stevens, D., & Mitchell, D. (2014). The effects of different sud-
544 den stratospheric warming types on the ocean. *Geophysical Research Letters*, *41*(21),
545 7739–7745.
- 546 O'Neill, A. (2003). Stratospheric sudden warmings. In J. R. Holton, J. A. Pyle, & J. A. Curry
547 (Eds.), *Encyclopedia of atmospheric sciences* (p. 1342-1353). Elsevier.
- 548 Osprey, S., Barnett, J., Smith, J., Adamson, P., Andreopoulos, C., Arms, K., ... others
549 (2009). Sudden stratospheric warmings seen in MINOS deep underground muon data.
550 *Geophysical Research Letters*, *36*(5).
- 551 Rosas-Carbajal, M., Jourde, K., Marteau, J., Deroussi, S., Komorowski, J.-C., & Gibert,
552 D. (2017). Three-dimensional density structure of La Soufrière de Guadeloupe lava
553 dome from simultaneous muon radiographies and gravity data. *Geophysical Research
554 Letters*, *44*(13), 6743–6751.
- 555 Scherhag, R. (1952). Die explosionartigen Stratosphärenwärmungen des Spätwinters 1951-
556 1952. *Ber. Deut. Wetterd.*, *6*, 51–63.
- 557 Schimanke, S., Spangehl, T., Huebener, H., & Cubasch, U. (2013). Variability and trends
558 of major stratospheric warmings in simulations under constant and increasing GHG
559 concentrations. *Climate Dynamics*, *40*(7-8), 1733–1747.
- 560 Sox, L., Wickwar, V. B., Fish, C. S., & Herron, J. P. (2016). Connection between the
561 midlatitude mesosphere and sudden stratospheric warmings as measured by Rayleigh-
562 scatter lidar. *Journal of Geophysical Research: Atmospheres*, *121*(9), 4627–4636.
- 563 Tanabashi, M., et al. (2018). (Particle Data Group). *Phys. Rev. D*, *98*(030001).
- 564 Thompson, D. W., Baldwin, M. P., & Wallace, J. M. (2002). Stratospheric connection
565 to Northern Hemisphere wintertime weather: Implications for prediction. *Journal of
566 Climate*, *15*(12), 1421–1428.
- 567 Vigorito, C. F., Selvi, M., Molinaro, A., Bruno, G., Trincherò, G., Fulgione, W., & Ghia,
568 P. (2017). Underground flux of atmospheric muons and its variations with 25 years of
569 data of the LVD experiment. *PoS*, 291.
- 570 Yuan, T., Thuraiajah, B., She, C.-Y., Chandran, A., Collins, R., & Krueger, D. (2012).
571 Wind and temperature response of midlatitude mesopause region to the 2009 sudden
572 stratospheric warming. *Journal of Geophysical Research: Atmospheres*, *117*(D9).

Figure 1.

Accepted Article



b)



Accepted Article

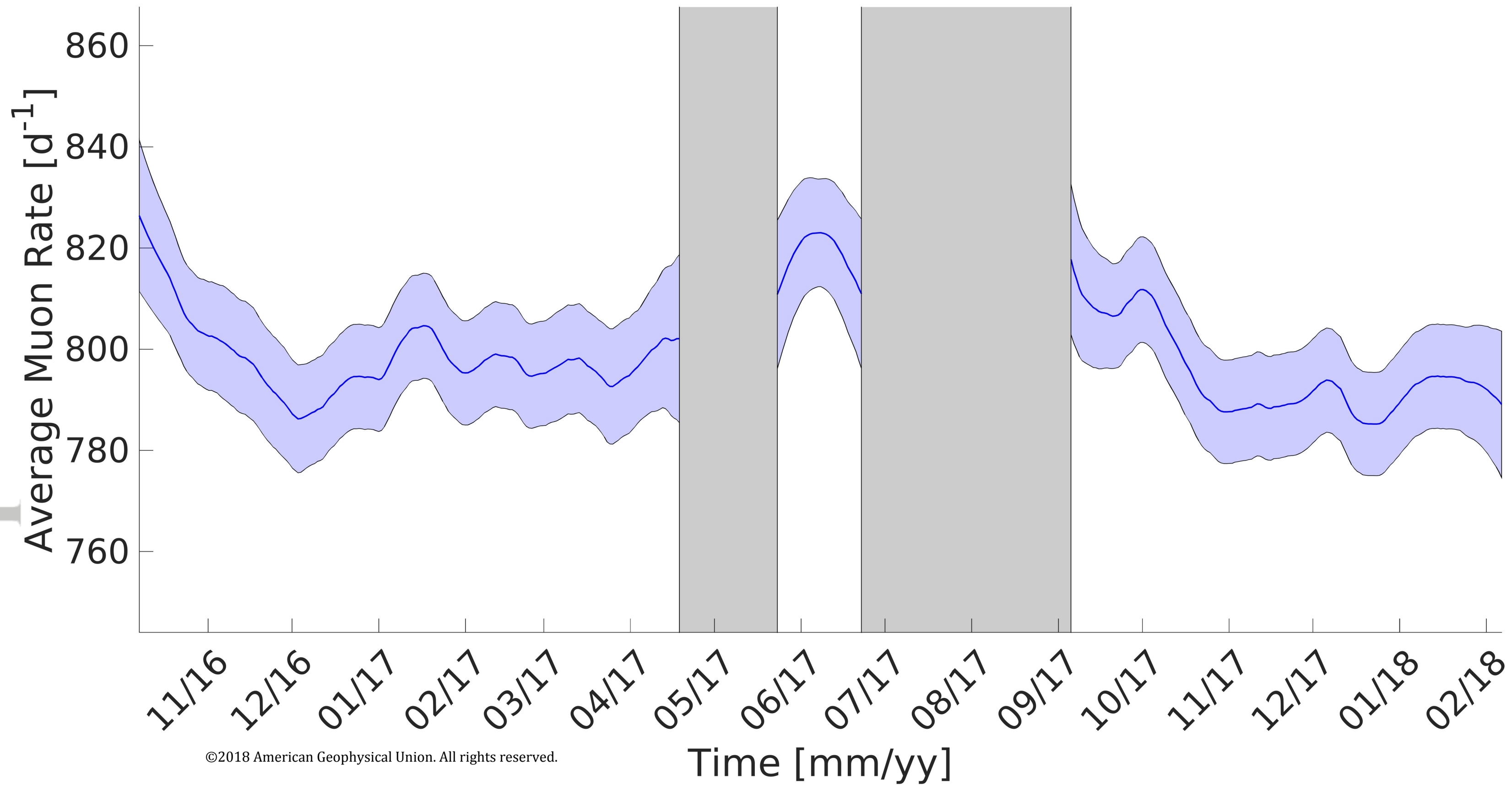
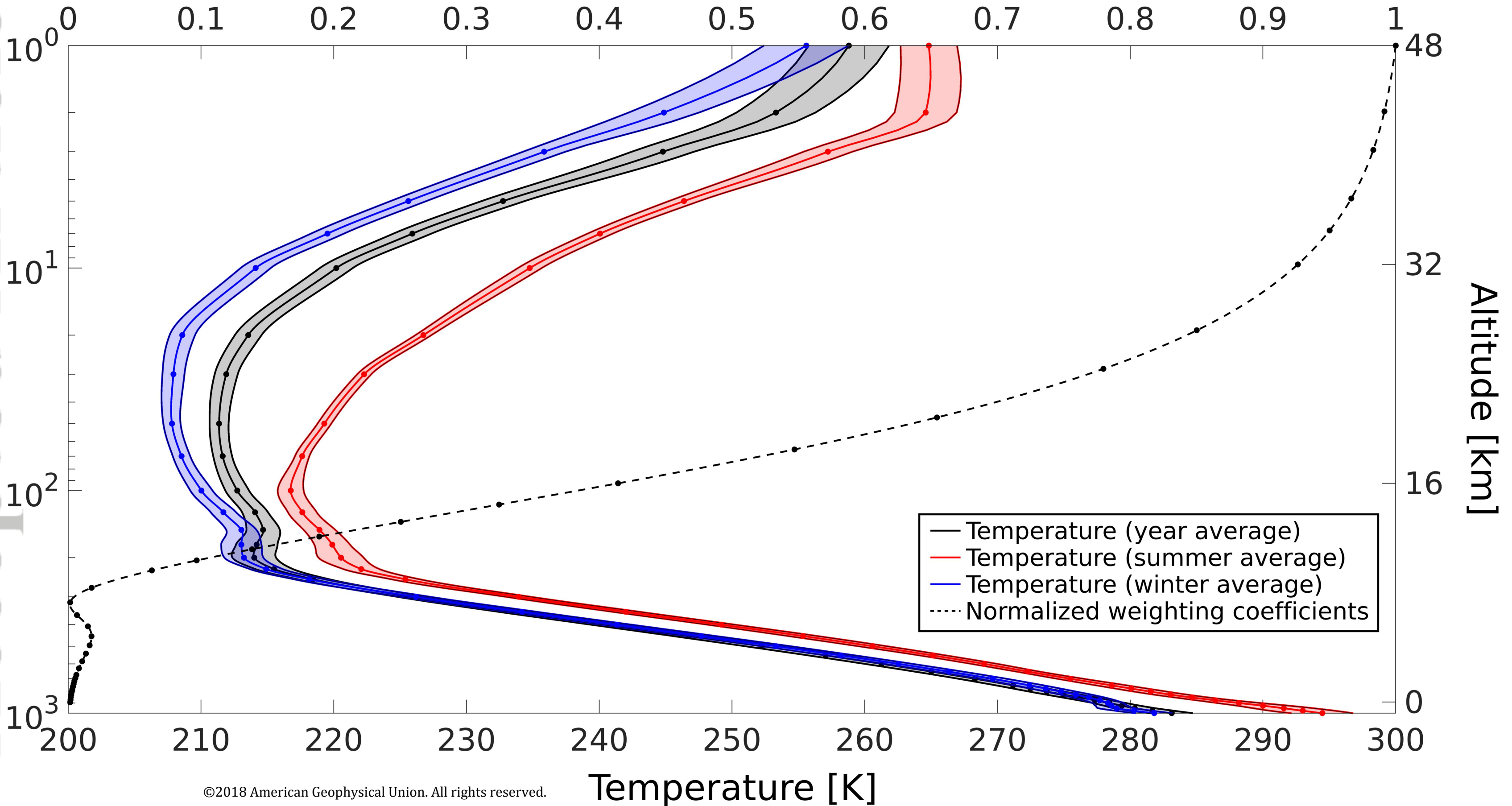


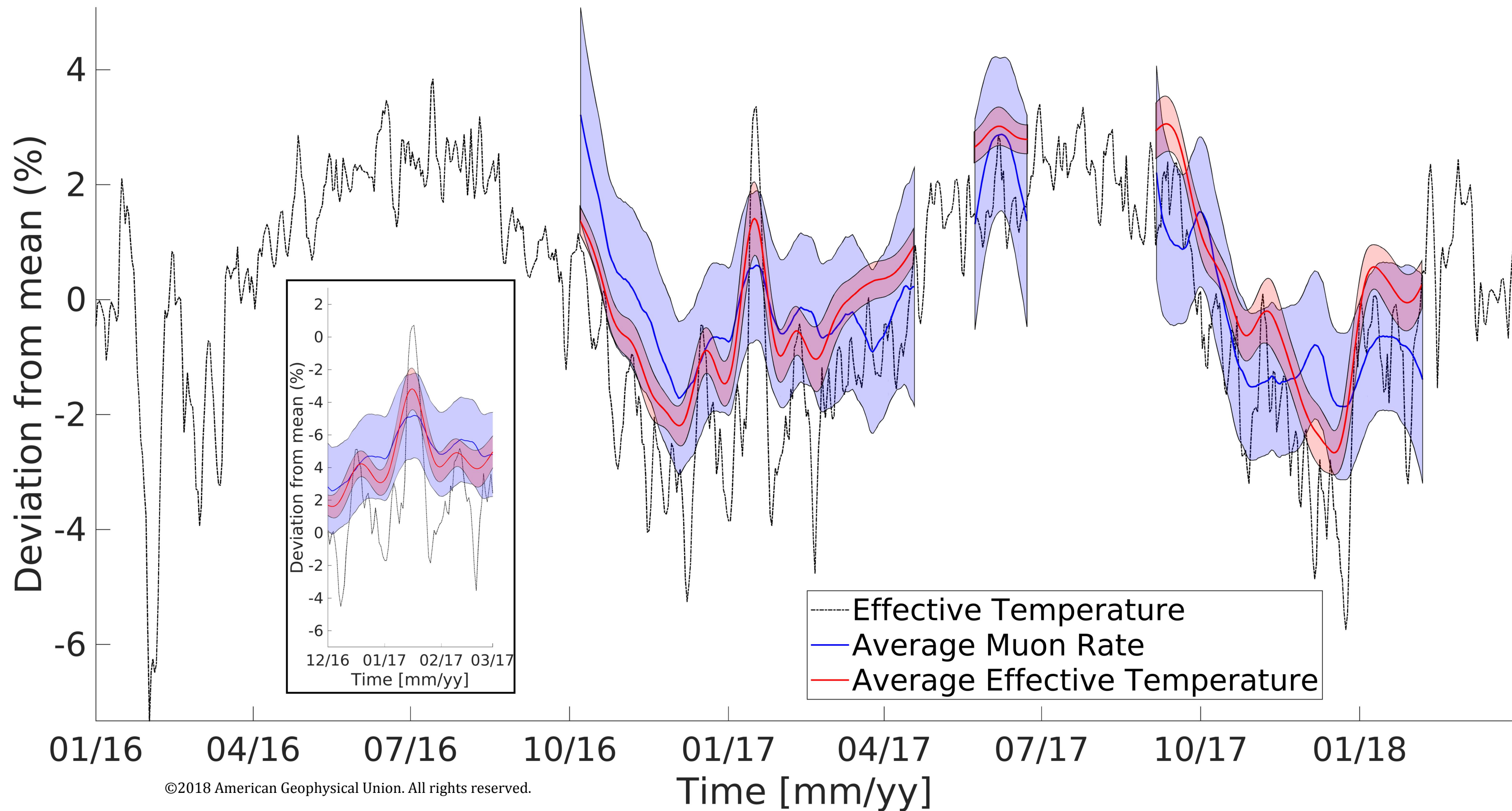
Figure 3.

Accepted Article

Normalized weighting coefficients



Accepted Article



Accepted Article

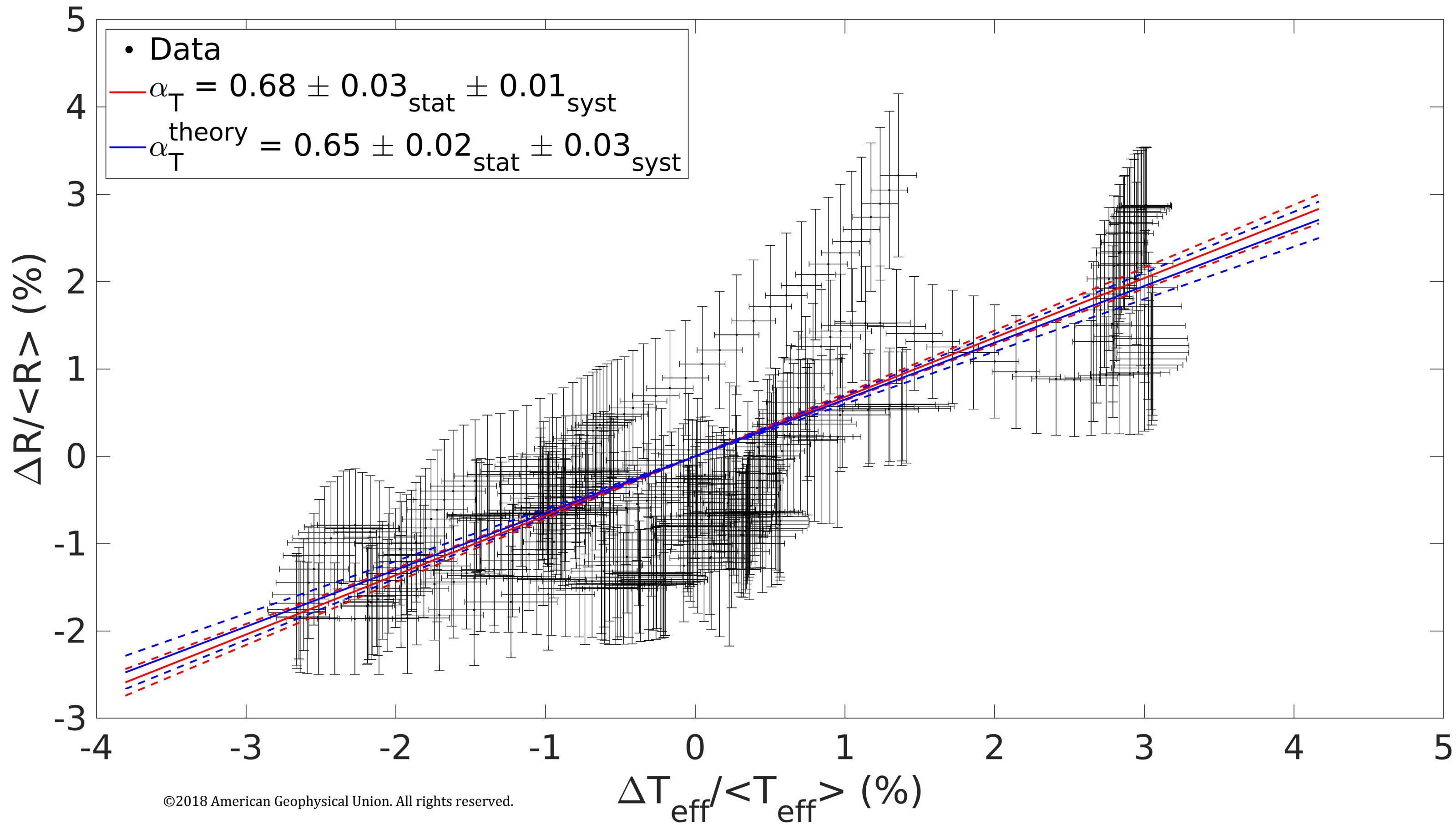
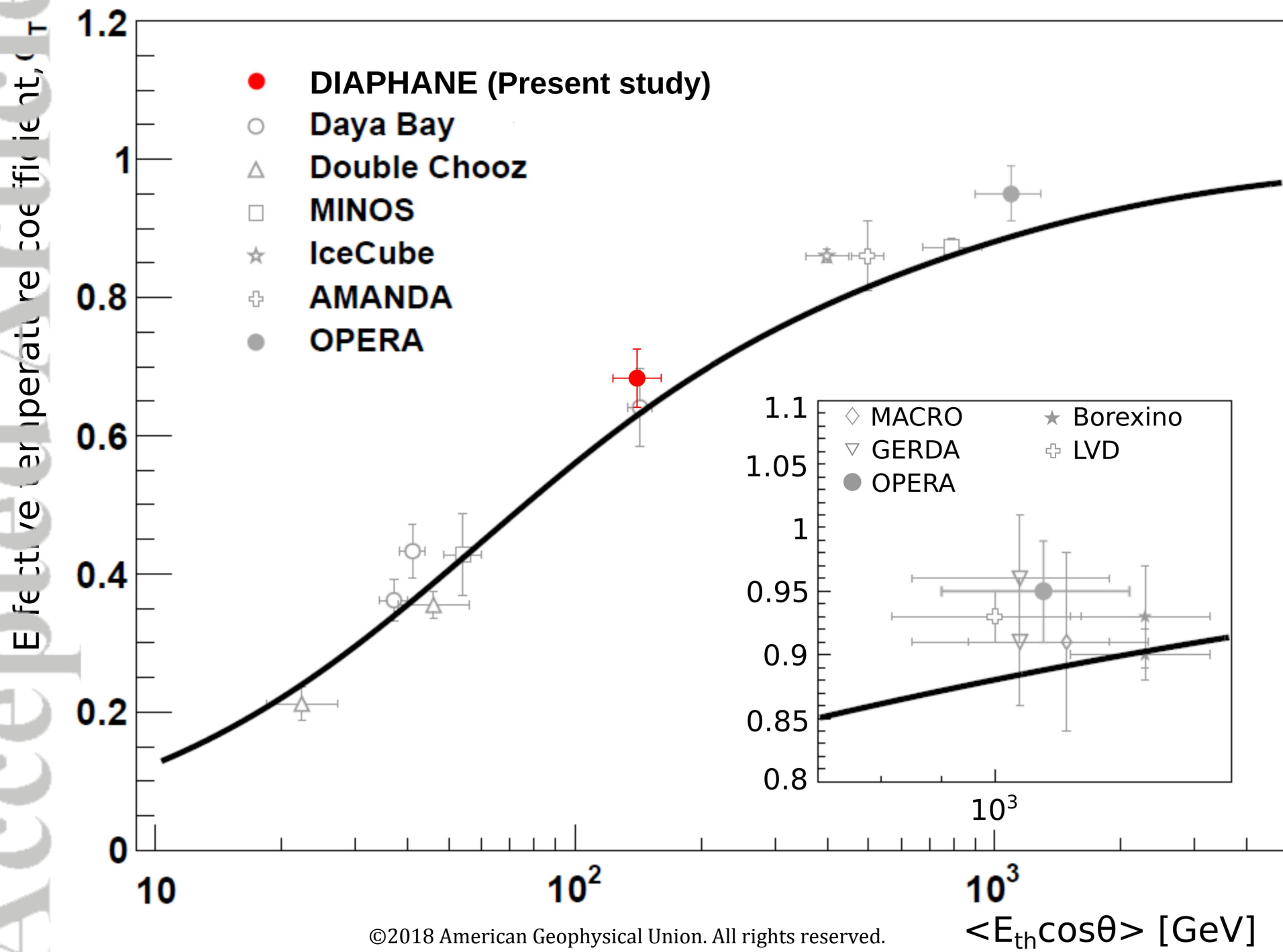


Figure 6.

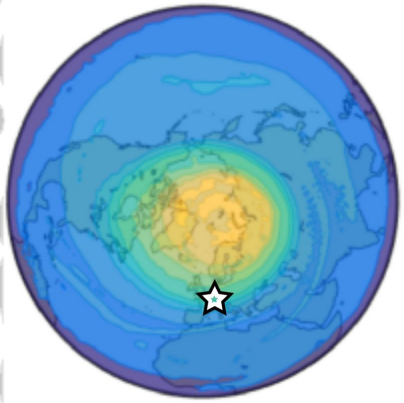
Accepted Article



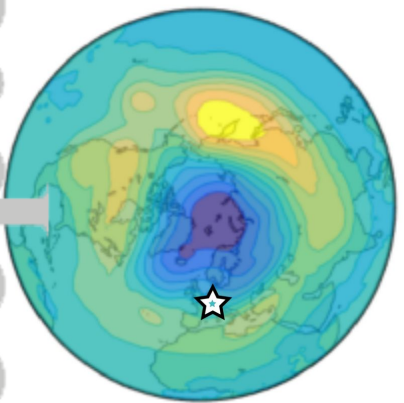
Accepted Article

a)

01-Jan-2017



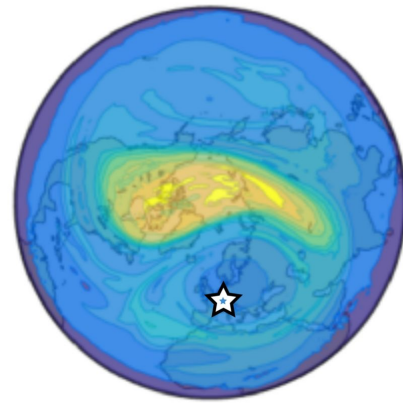
Potential Vorticity [PVU]



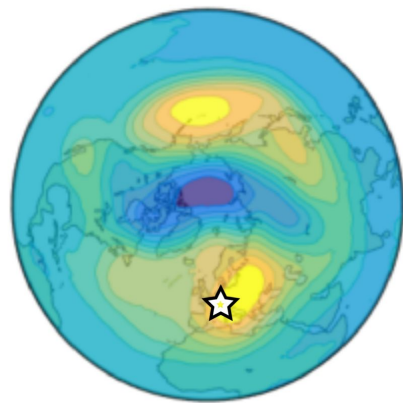
Effective Temperature [K]

b)

17-Jan-2017



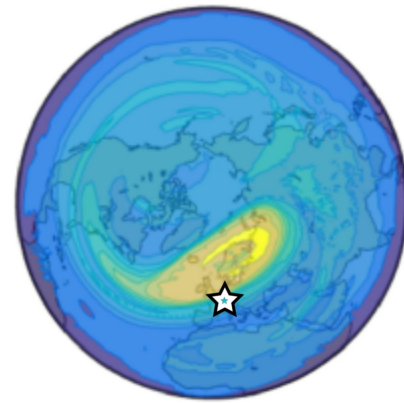
Potential Vorticity [PVU]



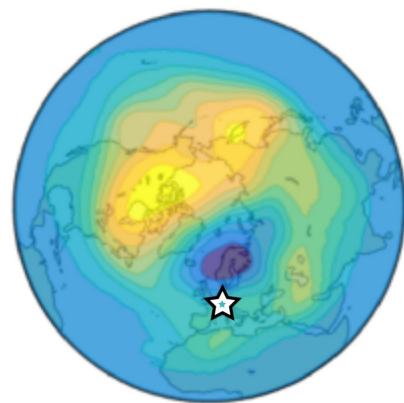
Effective Temperature [K]

c)

02-Feb-2017

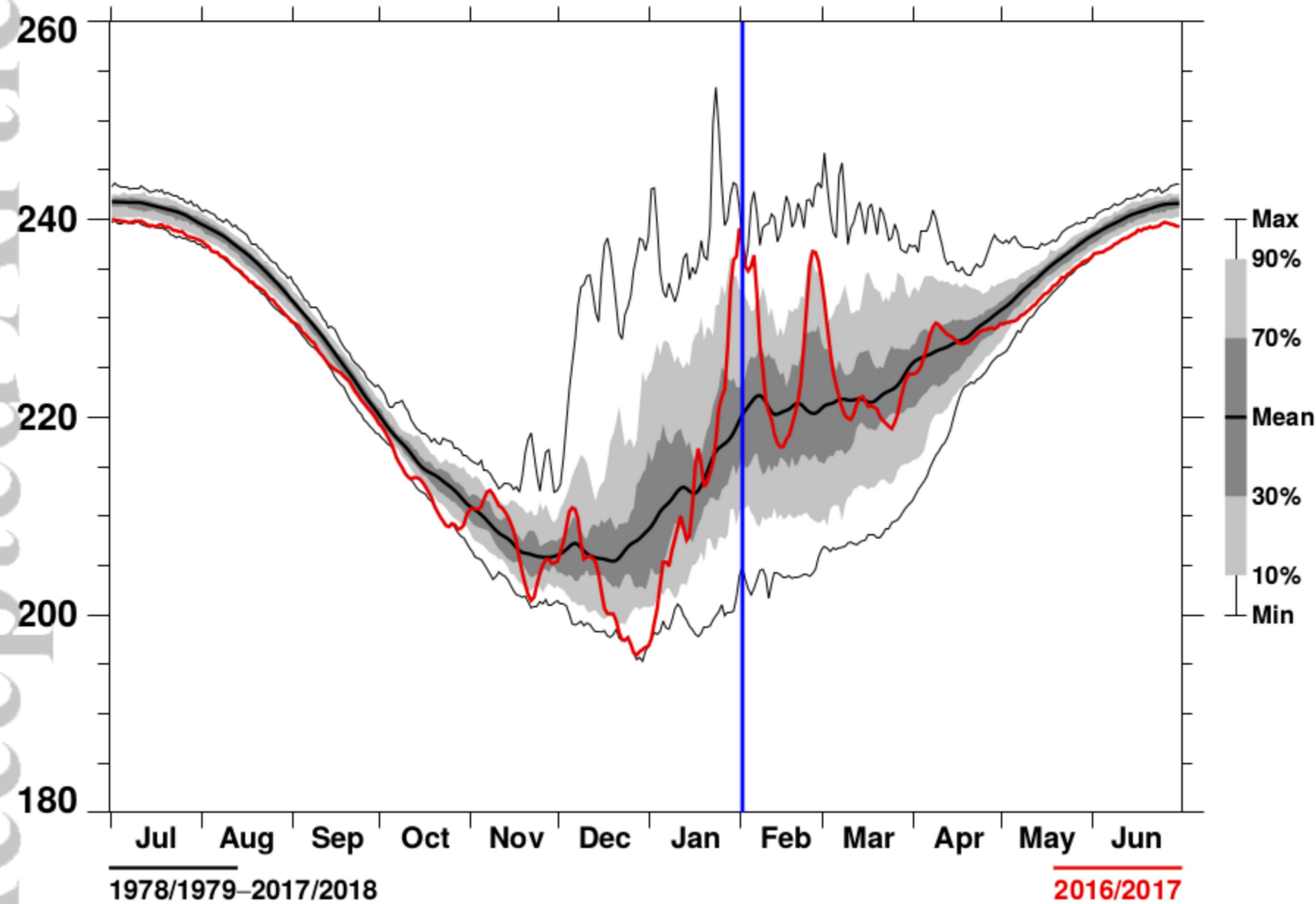


Potential Vorticity [PVU]

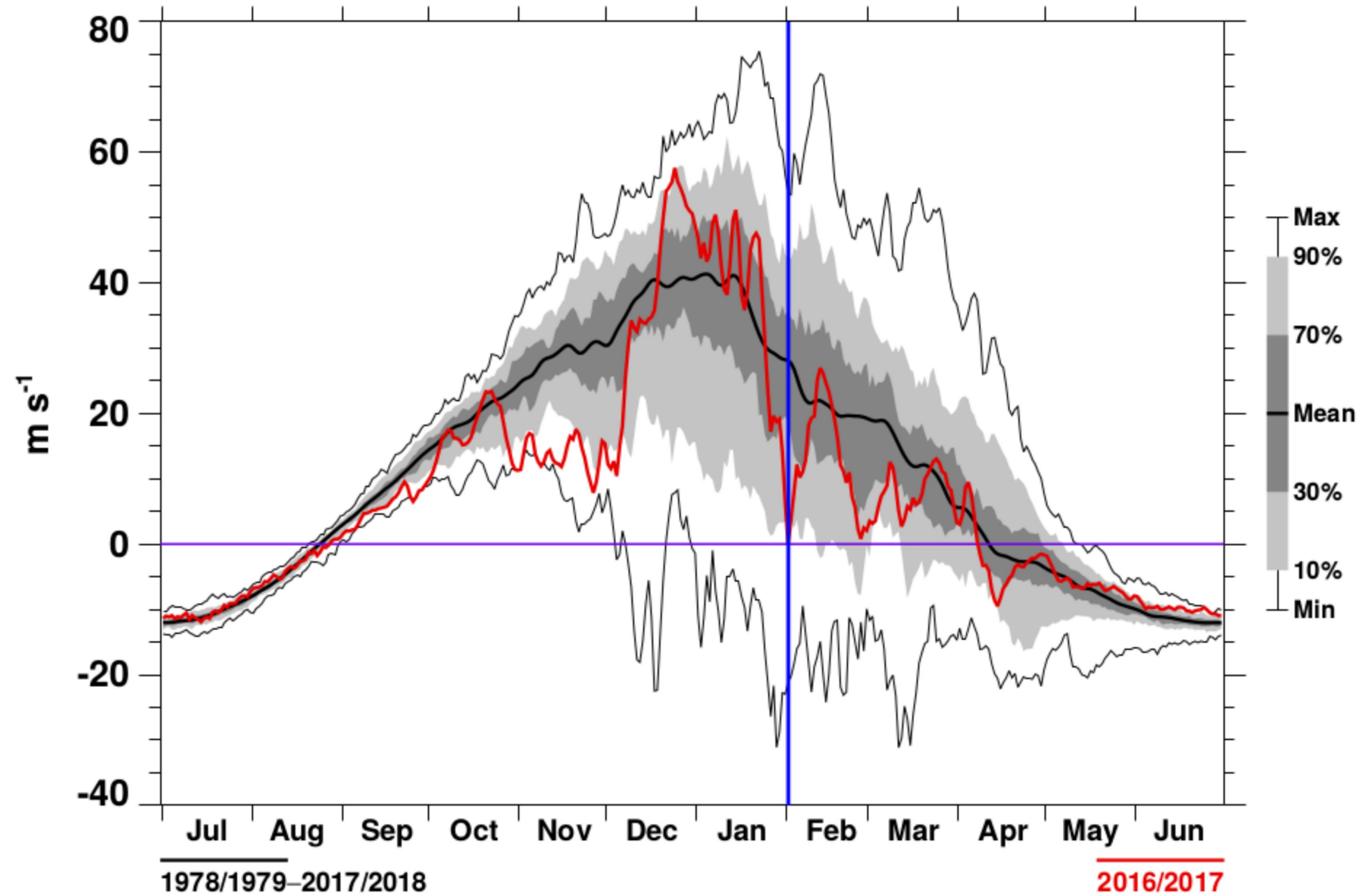


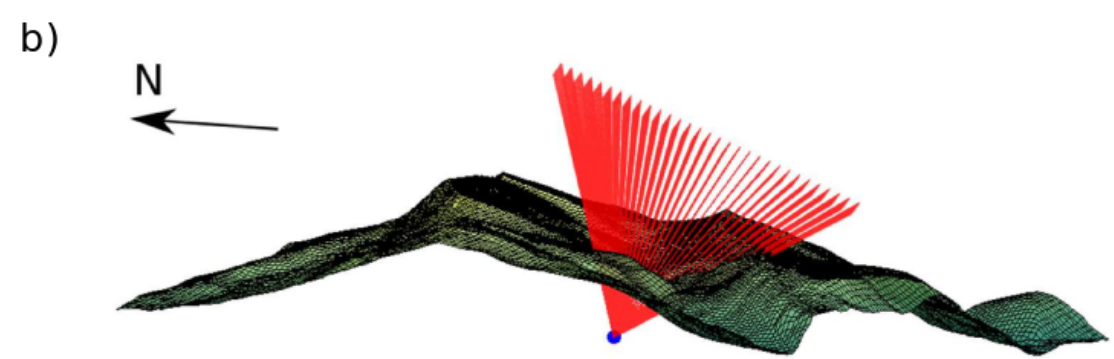
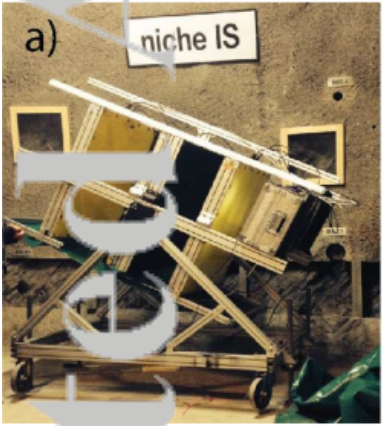
Effective Temperature [K]

Accepted Article

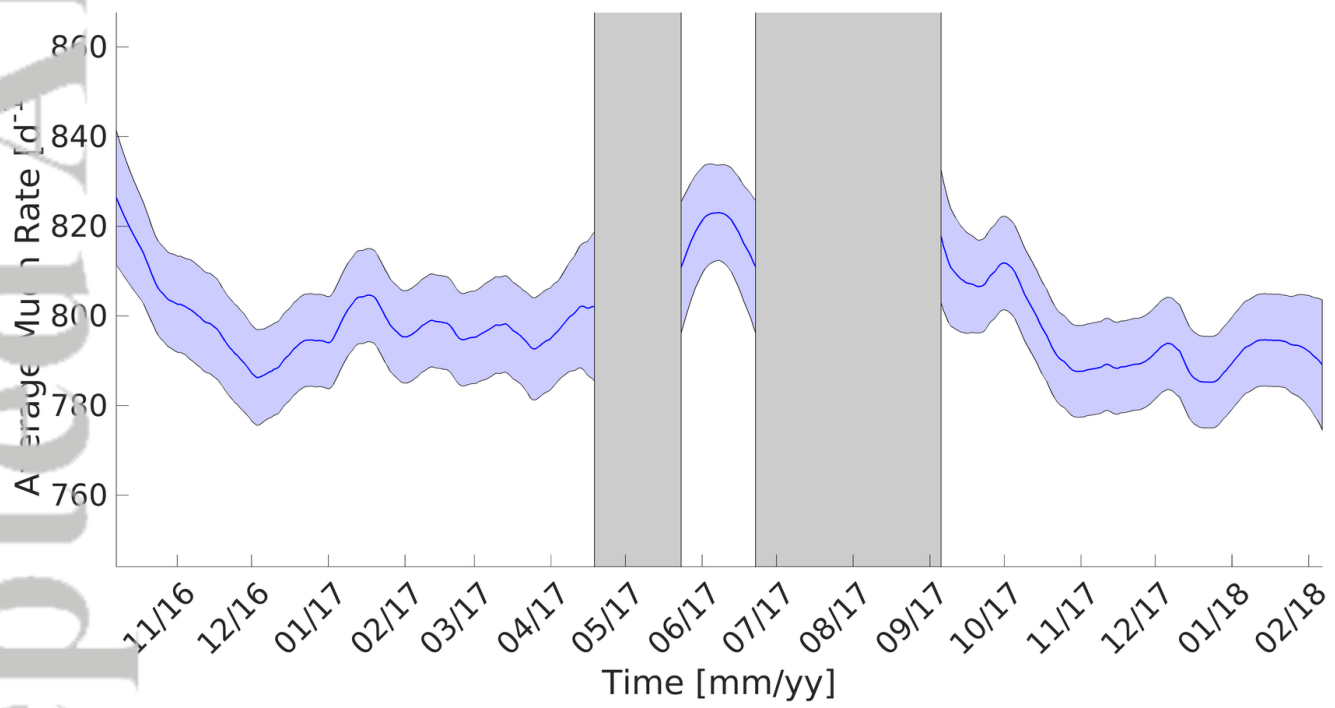
**60-90°N Zonal Mean Temperature
10 hPa MERRA2**

b)

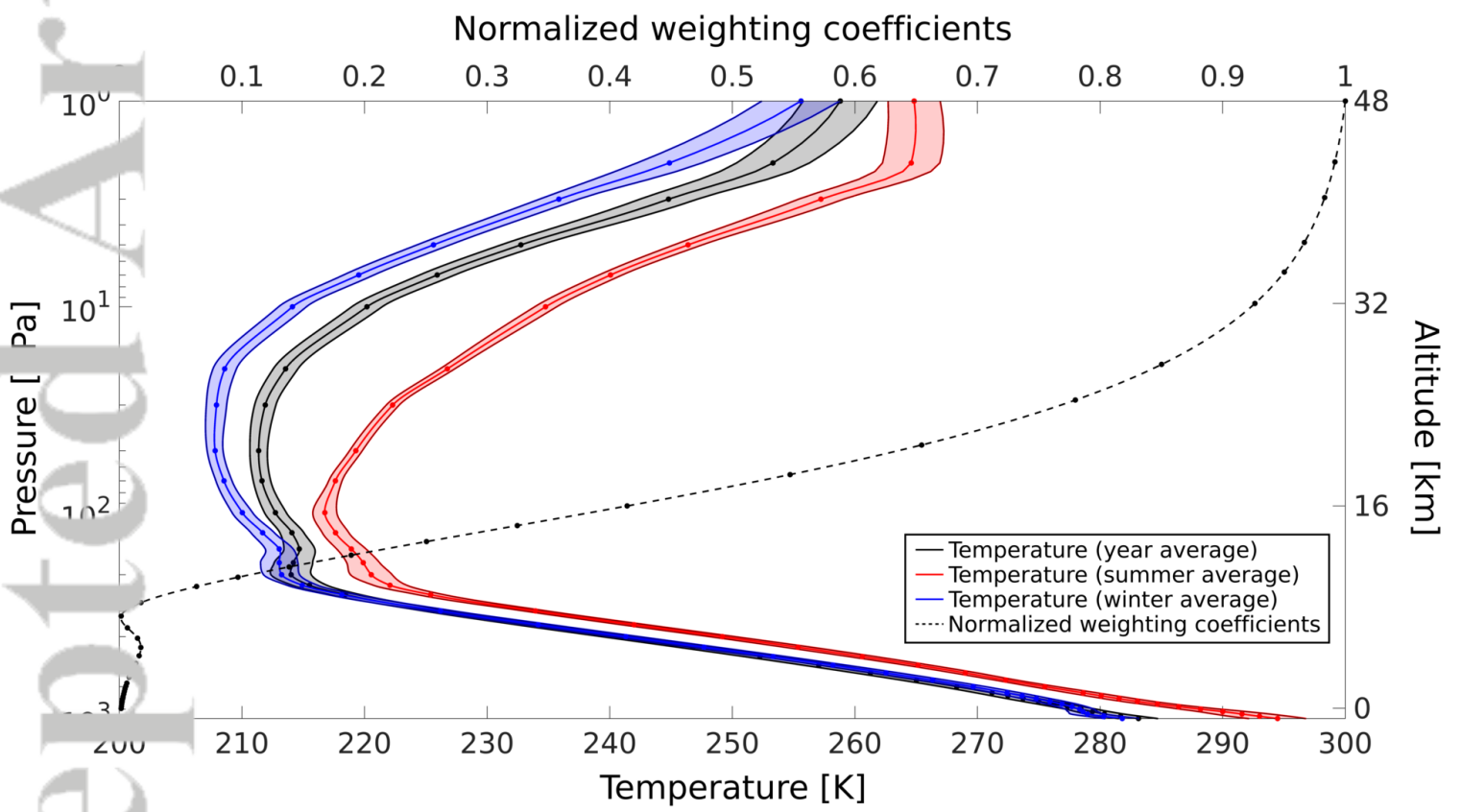
**60°N Zonal Mean Zonal Wind
10 hPa MERRA2**



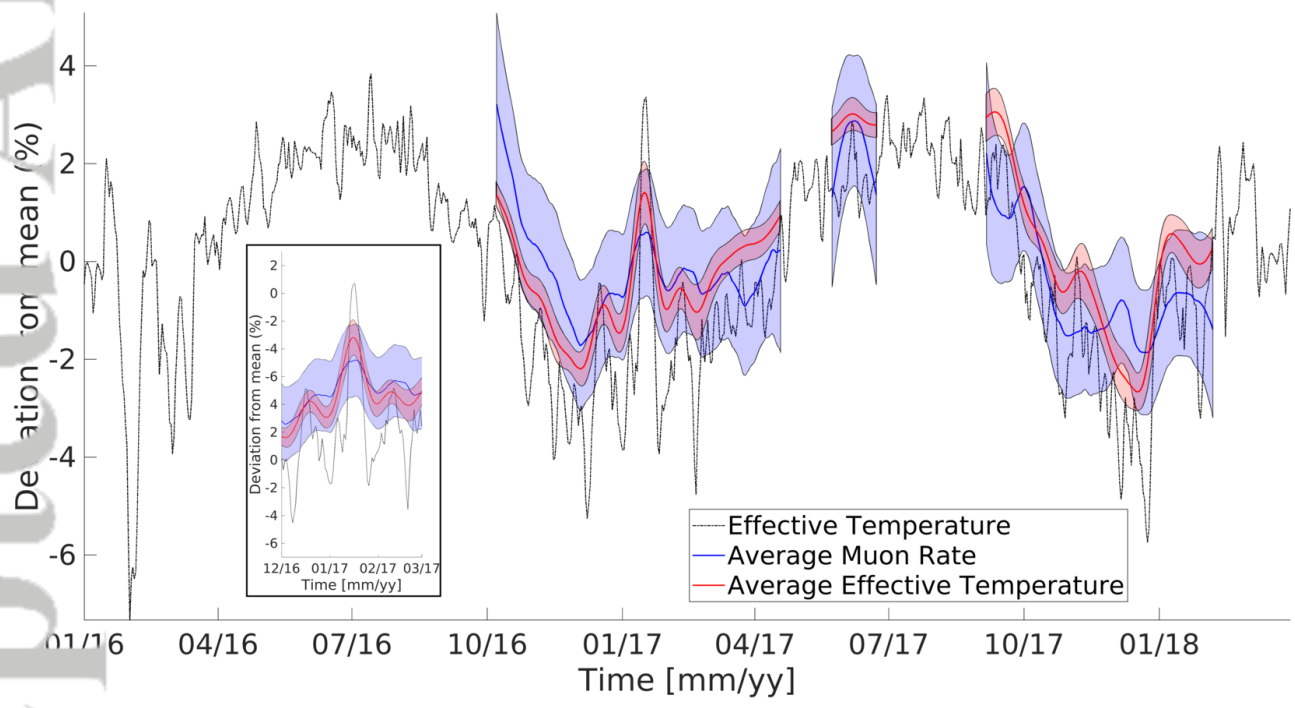
2019EA000655-f01-z-.png



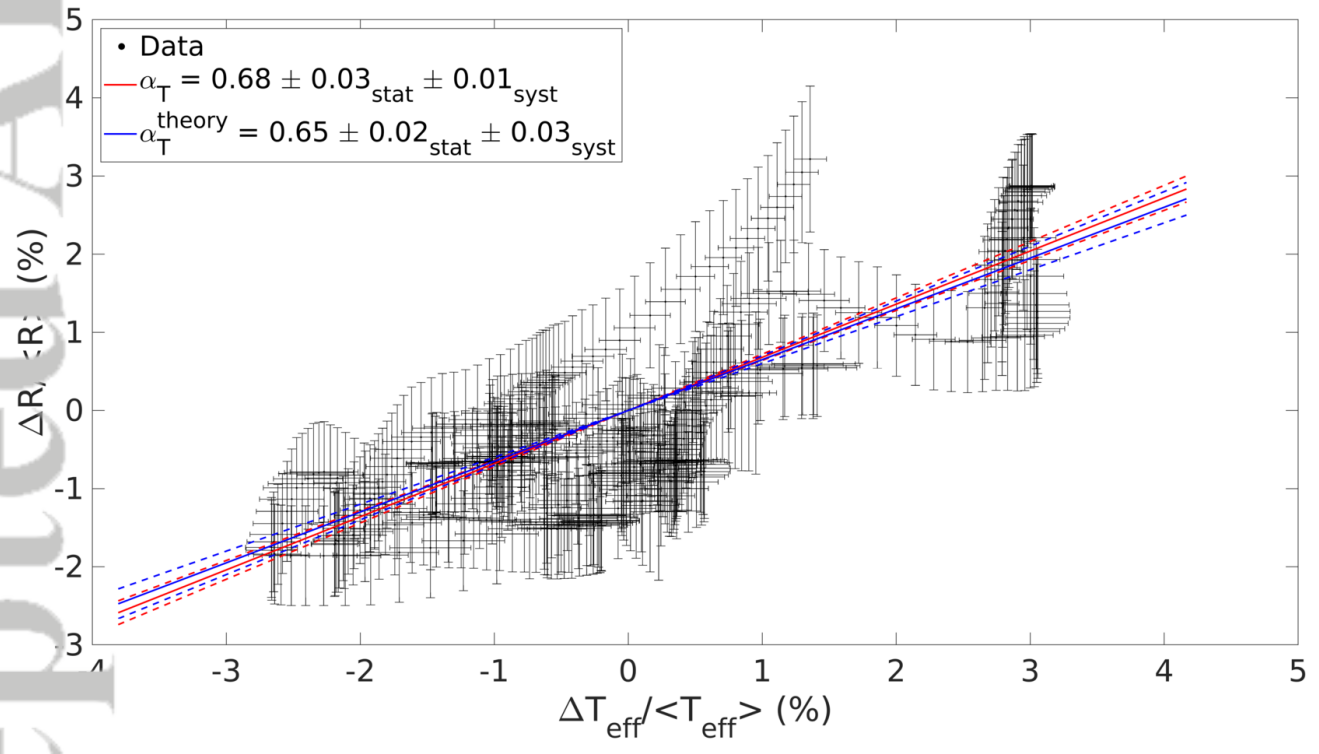
2019EA000655-f02-z.png



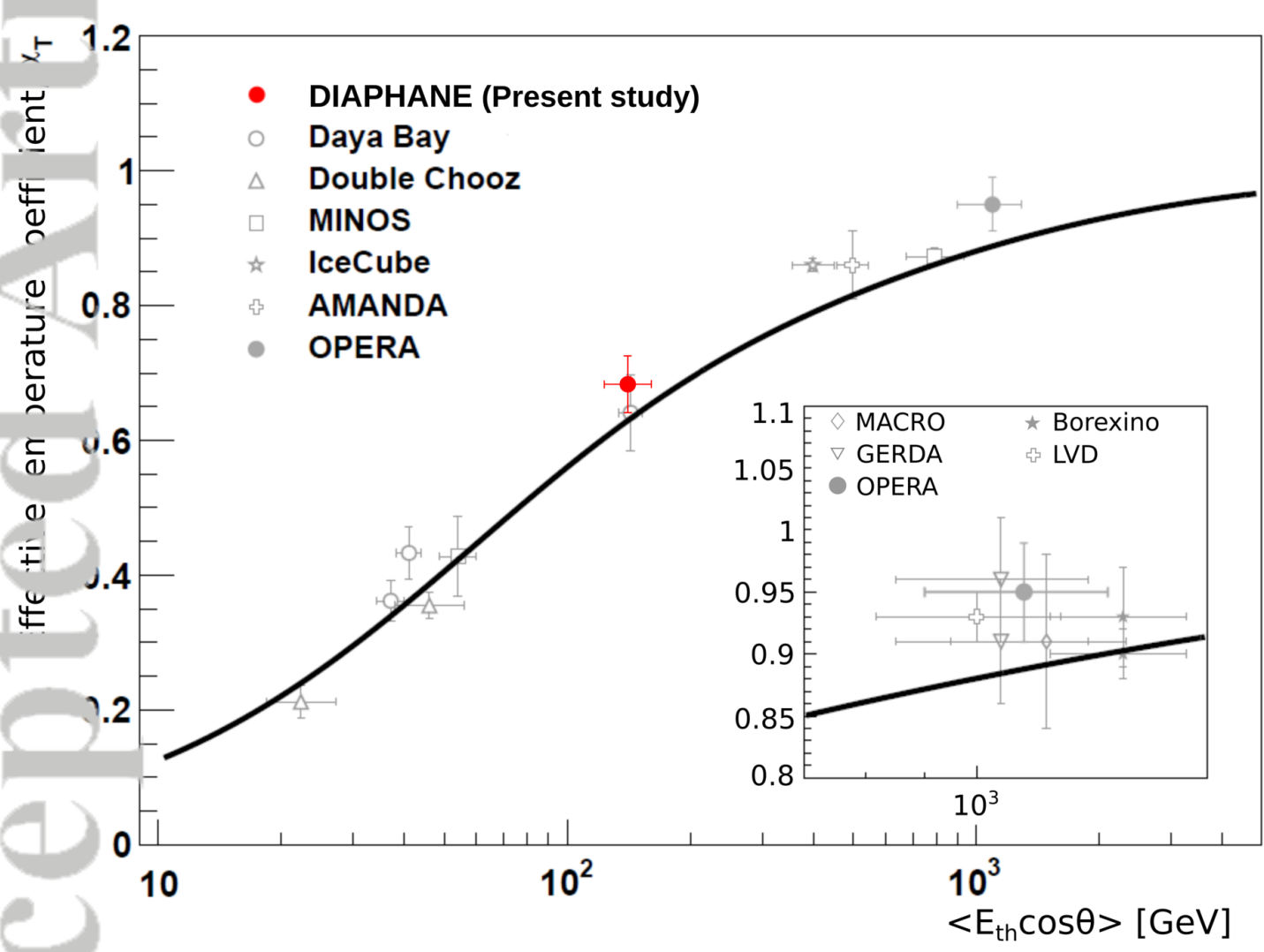
2019EA000655-f03-z-.png



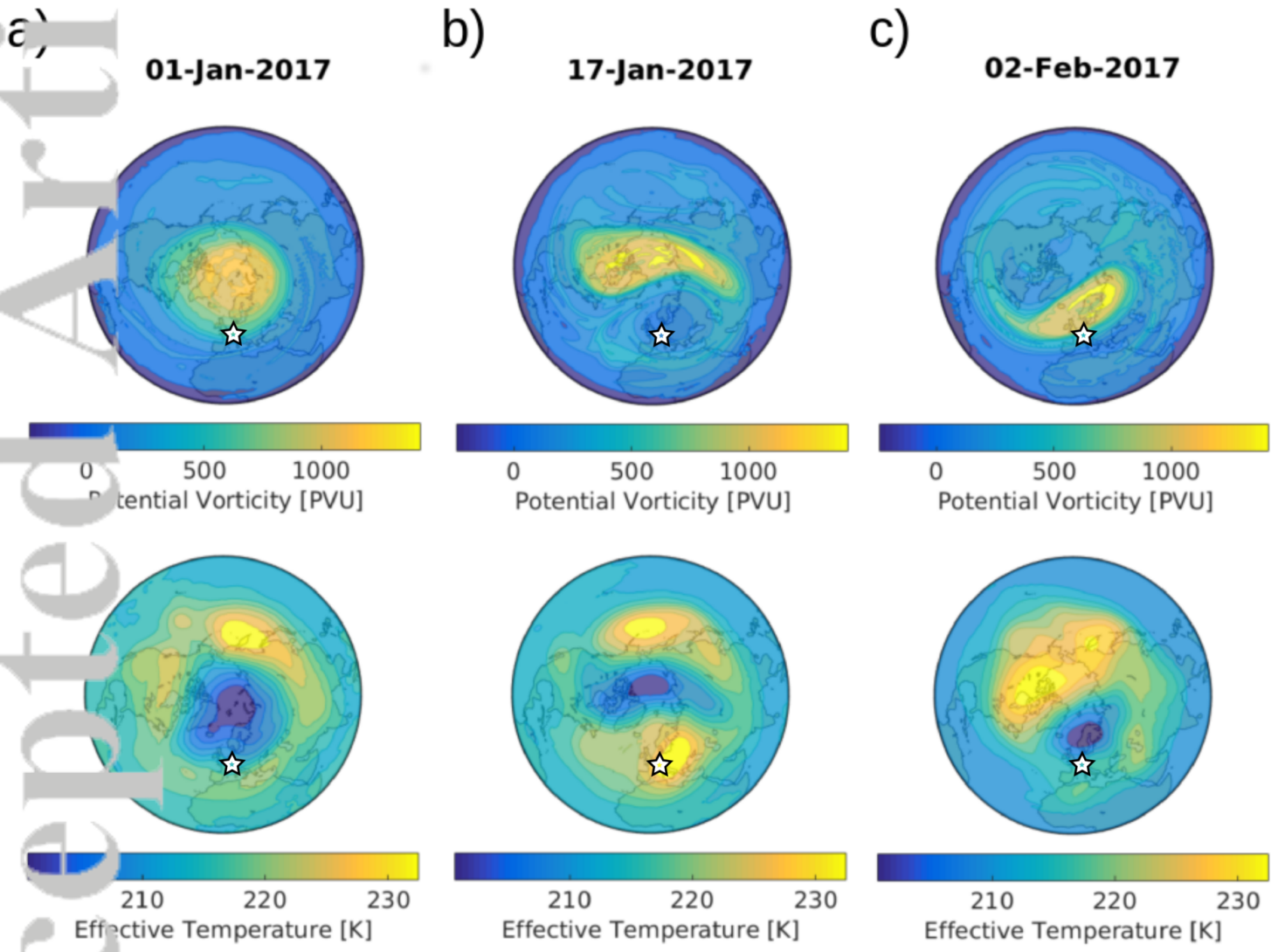
2019EA000655-f04-z.png



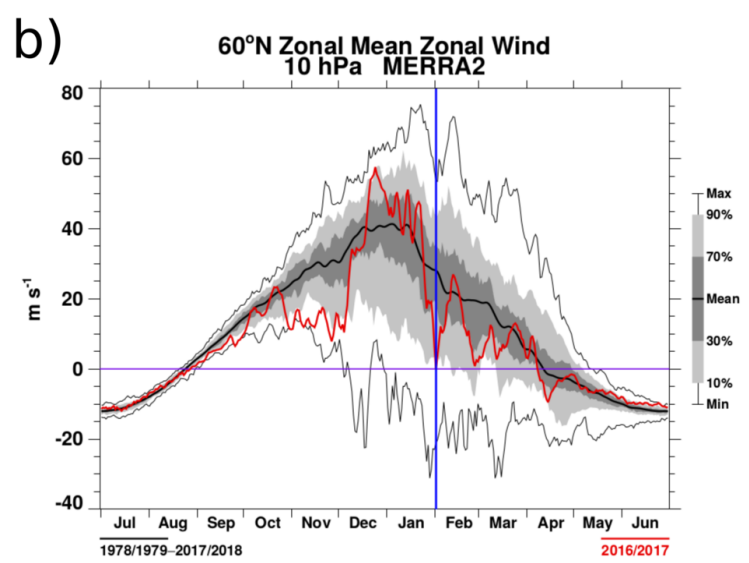
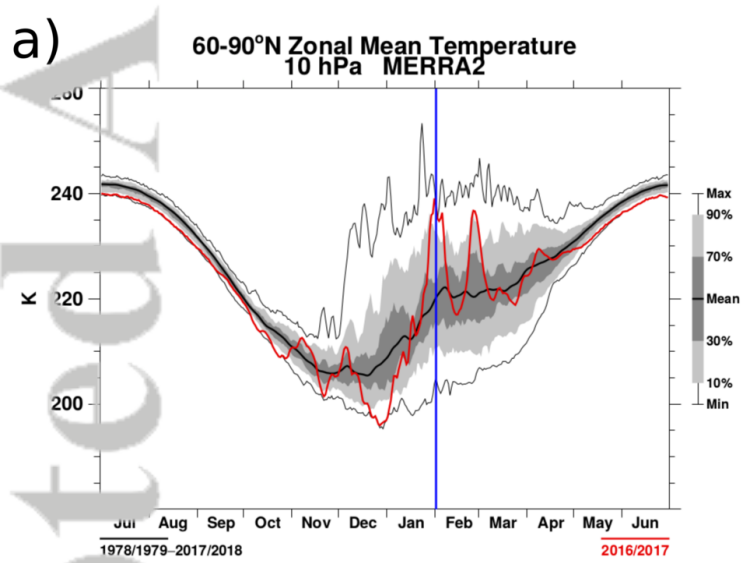
2019EA000655-f05-z-.png



2019EA000655-f06-z-.png



2019EA000655-f07-z-.png



2019EA000655-f08-z-.png